Journal of Magnetic Resonance 205 (2010) 181–195

Contents lists available at ScienceDirect

Journal of Magnetic Resonance

journal homepage: www.elsevier.com/locate/jmr

Pulsed-gradient spin-echo monitoring of restricted diffusion in multilayered structures

Denis S. Grebenkov

Laboratoire de Physique de la Matière Condensée, CNRS–Ecole Polytechnique, F-91128 Palaiseau, France

ARTICLE INFO

Article history:
Received 2 March 2010
Revised 26 April 2010
Available online 31 May 2010

Keywords:
Restricted diffusion
PGSE
Eigenfunction
Matrix formalism
Permeability

ABSTRACT

A general mathematical basis is developed for computation of the pulsed-gradient spin-echo signal attenuated due to restricted diffusion in multilayered structures (e.g., multiple slabs, cylindrical or spherical shells). Individual layers are characterized by (different) diffusion coefficients and relaxation times, while boundaries between adjacent layers are characterized by (different) permeabilities. Arbitrary temporal profile of the applied magnetic field can be incorporated. The signal is represented in a compact matrix form and the explicit analytical formulas for the elements of the underlying matrices are derived. The implemented algorithm is faster and much more accurate than classical techniques such as Monte Carlo simulations or numerical resolutions of the Bloch–Torrey equation. The algorithm can be applied for studying restricted diffusion in biological systems which exhibit a multilayered structure such as composite tissues, axons and living cells.

1. Introduction

A pulsed-gradient spin-echo (PGSE) technique is a non-invasive experimental tool for studying diffusive processes in mineral porous media and biological systems [1–4]. The past decade is marked by a significant increase in spatial resolution, image quality and acquisition rapidity that resulted in numerous clinical applications such as brain or lung imaging [5–10]. In turn, the progress in theoretical understanding of restricted diffusion in such complex systems is less spectacular. Although the theory is well established for few simple confining shapes (such as slab, cylinder and sphere) [11], its extension to heterogeneous media is essentially an open problem. Several phenomenological formulas (e.g., bi-exponential fit, stretched-exponential fit, etc.) are therefore used for fitting and interpreting measured signals in biological systems [12–18]. Physical and geometrical interpretation of fitting parameters, as well as the respective roles of various attenuation mechanisms (bulk and surface relaxation, permeation through boundaries, etc.), are still poorly understood in general.

We propose a general mathematical description of restricted diffusion in multilayered structures (Fig. 1), in which the Laplace operator eigenfunctions are known in a closed analytical form:

- multiple slabs separated by parallel planes (e.g., a model of composite or multilayered tissues);
- multiple cylindrical shells (e.g., a model of axons); and
- multiple spherical shells (e.g., a rough model of a living cell in which layers represent a nucleus, a cytoplasm, and an extracellular space).

Pulsed-gradient encoding of any temporal profile, individual bulk relaxivity and diffusivity for each layer, different permeabilities between adjacent layers, and exchange with an exterior space are rigorously included in this treatment. An efficient, accurate and rapid numerical tool for computing the signal attenuation is designed and implemented in Matlab. Since most computations are performed analytically, this matrix formalism significantly outperforms classical numerical methods such as Monte Carlo simulations.

The paper is organized as follows. Section 2 describes the mathematical basis of the spectral approach to restricted diffusion in multilayered structures. Although the formulas may look cumbersome and sophisticated, their practical implementation is straightforward. After all, restricted diffusion in multilayered structures is a complex phenomenon which needs an adequate description. In Section 2.1, the Bloch–Torrey equation is formulated for multilayered structures and its physical interpretation is recalled. Section 2.2 introduces the Laplace operator eigenfunctions. In Section 2.3, the computation of the Laplace operator eigenvalues is detailed. Section 2.4 summarizes the main steps of the matrix formalism. A practical implementation for multiple slabs, cylindrical and spherical shells is explained in Section 2.5. In Section 3, a practical use of the matrix formalism is illustrated by several examples. In particular, the role of the permeability of intermediate boundaries is investigated. Appendices describe the explicit

E-mail address: denis.grebenkov@polytechnique.edu

1090-7807/$ - see front matter © 2010 Elsevier Inc. All rights reserved.
doi:10.1016/j.jmr.2010.04.017

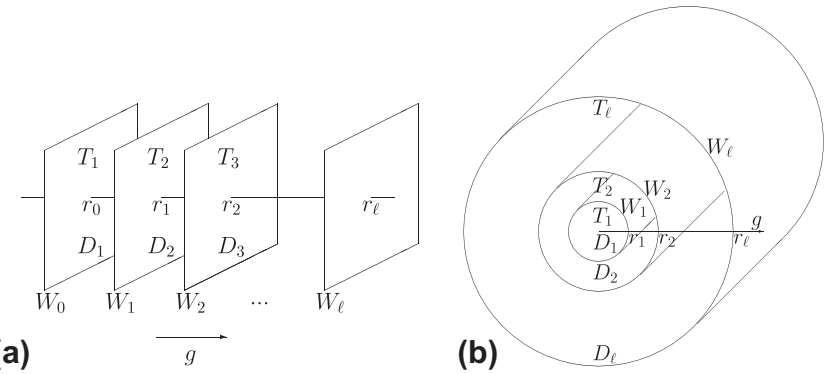

Fig. 1. Two examples of multilayered structures: (a) multiple slabs ($d = 1$) and (b) multiple cylindrical shells ($d = 2$).

formulas for the elements of the governing matrices. This is the key point for the performance of the matrix formalism.

2. Mathematical basis

2.1. Bloch–Torrey equation

We consider a multilayered domain $\Omega = \Omega_1 \cup \cdots \cup \Omega_\ell$, composed of ℓ layers $\Omega_i = \{\mathbf{r} \in \mathbb{R}^d : r_{i-1} < |\mathbf{r}| < r_i\}$, with $r_0 < r_1 < \cdots < r_\ell = R$ (Fig. 1). Each layer Ω_i is characterized by diffusion coefficient D_i and relaxation time T_i (representing transverse spin-spin relaxation). The inner, outer and each intermediate boundary, $\Gamma_i = \{\mathbf{r} \in \mathbb{R}^d : |\mathbf{r}| = r_i\}$ $(i = 0 \ldots \ell)$, is characterized by permeability W_i. For such a composite system, the classical Bloch–Torrey equation becomes:

$$\begin{aligned}
&\left(\frac{\partial}{\partial t} - D_i\Delta + i\omega f(t)B(\mathbf{r}) + T_i^{-1}\right)m_i(\mathbf{r},t) = 0 \quad (\mathbf{r} \in \Omega_i, i = 1 \ldots \ell),\\
&D_i\frac{\partial}{\partial n}m_i(\mathbf{r},t) = -D_{i+1}\frac{\partial}{\partial n}m_{i+1}(\mathbf{r},t) \quad (\mathbf{r} \in \Gamma_i, i = 1 \ldots \ell - 1),\\
&D_i\frac{\partial}{\partial n}m_i(\mathbf{r},t) = W_i[m_{i+1}(\mathbf{r},t) - m_i(\mathbf{r},t)] \quad (\mathbf{r} \in \Gamma_i, i = 1 \ldots \ell - 1),\\
&D_\ell\frac{\partial}{\partial n}m_\ell(\mathbf{r},t) = -W_\ell m_\ell(\mathbf{r},t) \quad (\mathbf{r} \in \Gamma_\ell),\\
&D_1\frac{\partial}{\partial n}m_1(\mathbf{r},t) = -W_0 m_1(\mathbf{r},t) \quad (\mathbf{r} \in \Gamma_0),
\end{aligned} \tag{1}$$

where $m_i(\mathbf{r},t)$ is the transverse magnetization inside the ith layer, $\Delta = \partial^2/\partial x_1^2 + \cdots + \partial^2/\partial x_d^2$ is the d-dimensional Laplace operator acting on $\mathbf{r} = (x_1,\ldots,x_d)$, $\partial/\partial n$ is the normal derivative on the boundary pointing to the exterior of the domain, and ω is the Larmor frequency associated with an applied magnetic field of a given (dimensionless) temporal profile $f(t)$ and of spatial variation $B(\mathbf{r})$.

The first equation states that the time evolution of the magnetization is caused by

- local random displacements of the spin-bearing particles, i.e., diffusion which is governed by the Laplace operator,
- encoding through the applied magnetic field, and
- bulk relaxations.

The second equation describes the conservation of the flux of magnetization between adjacent layers (the sign minus accounts for the opposite directions of two normal derivatives at the intermediate boundary Γ_i). The third equation accounts for the transfer properties (permeabilities W_i) of intermediate boundaries. It states that the diffusive flux is created by the drop in magnetization between two layers. For biological samples, typical water permeabilities are in the order of 10^{-5} m/s (e.g., for axons [19,20]). Finally, the last two equations describe the flux conservation at the outer and inner boundaries Γ_ℓ and Γ_0, respectively. If there is no inner boundary (Fig. 1b), the last equation is replaced by the condition of a regularity of $m(\mathbf{r},t)$ at the origin.

The above mathematical description is approximate. The underlying assumptions are:

- All the intermediate boundaries are infinitely thin. When such an approximation is not adequate, the frontier between two layers (e.g., a cellular membrane) can be modeled itself as an intermediate layer, with an effective diffusion coefficient and appropriate relaxation time.
- Although surface relaxation is formally neglected, it can be easily taken into account. For the outer and inner boundaries, the transport coefficients W_ℓ and W_0 represent the losses of the spin-bearing particles which leave the multilayered structure. But the very same constants W_ℓ and W_0 may also account for surface relaxation on the outer and inner boundaries. If surface relaxation at intermediate boundaries is also relevant, these infinitely thin boundaries can be replaced by additional intermediate layers for which surface relaxation can be effectively incorporated through the corresponding bulk relaxation times.
- The third equation relates the diffusive flux to the drop of magnetization between two layers. This is an effective model for describing transfer properties of a membrane. Another model relates the magnetizations at the edges of two layers by a linear relation, namely, $m_i(\mathbf{r},t) = w_i m_{i+1}(\mathbf{r},t)$ (as $\mathbf{r} \in \Gamma_i$), with a dimensionless constant w_i. The approach we present can be easily adapted to this model. At the same time, it is known that cellular membranes transfer species via different mechanisms (e.g., active transfer of some macromolecules [21,22]) which may result in more sophisticated equations. This paper is focused only on linear boundary conditions in Eq. (1).
- The Brownian dynamics of the spin-bearing particles is not always valid for biological systems. For instance, the dynamics of proteins and other macromolecules inside living cells is often anomalous [23–26]. Anomalous diffusion or other intricate dynamics are beyond the scope of the paper.

In what follows, we assume that a PGSE experiment is accurately described by Eq. (1).

2.2. Laplace operator eigenfunctions

A solution of the Bloch–Torrey Eq. (1) can be written in terms of the Laplace operator eigenfunctions [11,27,28]. For multilayered structures, each eigenfunction $u(\mathbf{r})$ satisfies the following equations:

$$D_i\Delta u_i(\mathbf{r}) + \lambda u_i(\mathbf{r}) = 0 \quad (\mathbf{r}\in\Omega_i, i = 1\dots\ell), \tag{2}$$

$$D_i\frac{\partial}{\partial n}u_i(\mathbf{r}) = -D_{i+1}\frac{\partial}{\partial n}u_{i+1}(\mathbf{r}) \quad (\mathbf{r}\in\Gamma_i, i = 1\dots\ell-1), \tag{3}$$

$$D_i\frac{\partial}{\partial n}u_i(\mathbf{r}) = W_i[u_{i+1}(\mathbf{r}) - u_i(\mathbf{r})] \quad (\mathbf{r}\in\Gamma_i, i = 1\dots\ell-1), \tag{4}$$

$$D_\ell\frac{\partial}{\partial n}u_\ell(\mathbf{r}) = -W_\ell u_\ell(\mathbf{r}) \quad (\mathbf{r}\in\Gamma_\ell), \tag{5}$$

$$D_1\frac{\partial}{\partial n}u_1(\mathbf{r}) = -W_0 u_1(\mathbf{r}) \quad (\mathbf{r}\in\Gamma_0), \tag{6}$$

where λ is the associated eigenvalue (in units s^{-1}), and $u_i(\mathbf{r})$ is the restriction of the eigenfunction $u(\mathbf{r})$ on the ith layer Ω_i. When there is no inner boundary, the last equation is replaced by the condition of regularity of $u(\mathbf{r})$ at the origin.

In spherical coordinates, the Laplace operator is

$$\Delta = \frac{1}{r^{d-1}}\frac{\partial}{\partial r}\left(r^{d-1}\frac{\partial}{\partial r}\right) + \frac{\Delta_{\text{ang}}}{r^2}, \tag{7}$$

where Δ_{ang} is the Laplace–Beltrami operator in angular coordinates [29]. For rotation-invariant domains, the radial and angular dependences of a Laplace operator eigenfunction are factored, $u(\mathbf{r}) = v(r)w(\theta,\dots)$, and the eigenvalue Eq. (2) splits in two separate equations

$$\Delta_{\text{ang}}w(\theta,\dots) + \nu w(\theta,\dots) = 0, \tag{8}$$

$$(r^{d-1}v')' + \left[(\lambda/D_i)r^{d-1} - \nu r^{d-3}\right]v = 0 \quad (r_i < r < r_{i+1}), \tag{9}$$

where the prime denotes the derivative with respect to the radial coordinate r. Since the normal derivative $\partial/\partial n$ is simply $\pm\partial/\partial r$, Eqs. (3) and (4) at the intermediate boundaries can be conveniently written as

$$\begin{aligned} &D_i v_i'(r_i) + W_i v_i(r_i) = W_i v_{i+1}(r_i),\\ &W_i v_i(r_i) = W_i v_{i+1}(r_i) - D_{i+1}v_{i+1}'(r_i), \end{aligned} \tag{10}$$

where $v_i(r)$ is the restriction of $v(r)$ on the interval (r_i, r_{i+1}).

2.3. Computation of the eigenvalues

A general form of a solution of Eq. (9) is a linear combination of its two independent solutions that can be denoted $J(r)$ and $Y(r)$ (see Section 2.5):

$$v_i(r) = b_i J\left(r\sqrt{\lambda/D_i}\right) + c_i Y\left(r\sqrt{\lambda/D_i}\right). \tag{11}$$

The $2\ell+1$ unknowns (ℓ pairs $\{b_i, c_i\}$ and λ) can be found by using $2(\ell-1)$ Eqs. (3) and (4) at $\ell-1$ intermediate boundaries, two Eqs. (5) and (6) at the outer and inner boundaries, and one normalization condition for the eigenfunction.

Denoting $\rho_i = r_i/\sqrt{D_i}$, $\tilde\rho_i = r_i/\sqrt{D_{i+1}}$, and $\alpha = \sqrt{\lambda}$, one can write the boundary conditions (10) as matrix relations for the unknown coefficients b_i,c_i:

$$\begin{pmatrix} \alpha\sqrt{D_i}J'(\alpha\rho_i) + W_i J(\alpha\rho_i) & \alpha\sqrt{D_i}Y'(\alpha\rho_i) + W_i Y(\alpha\rho_i)\\ W_i J(\alpha\rho_i) & W_i Y(\alpha\rho_i)\end{pmatrix}\begin{pmatrix} b_i\\ c_i\end{pmatrix}$$
$$= \begin{pmatrix} W_i J(\alpha\tilde\rho_i) & W_i Y(\alpha\tilde\rho_i)\\ W_i J(\alpha\tilde\rho_i) - \alpha\sqrt{D_{i+1}}J'(\alpha\tilde\rho_i) & W_i Y(\alpha\tilde\rho_i) - \alpha\sqrt{D_{i+1}}Y'(\alpha\tilde\rho_i)\end{pmatrix}\begin{pmatrix} b_{i+1}\\ c_{i+1}\end{pmatrix},$$

from which

$$\begin{pmatrix} b_{i+1}\\ c_{i+1}\end{pmatrix} = A_i(\alpha)\begin{pmatrix} b_i\\ c_i\end{pmatrix}, \tag{12}$$

where the elements of the 2×2 matrix $A_i(\alpha)$ are

$$\begin{aligned}
[A_i(\alpha)]_{11} &= Q_i(\alpha)\Big[-\sqrt{D_i/D_{i+1}}J'(\alpha\rho_i)Y(\alpha\tilde\rho_i) + J(\alpha\rho_i)Y'(\alpha\tilde\rho_i)\\
&\quad + W_i^{-1}\sqrt{D_i}\alpha J'(\alpha\rho_i)Y'(\alpha\tilde\rho_i)\Big],\\
[A_i(\alpha)]_{12} &= Q_i(\alpha)\Big[-\sqrt{D_i/D_{i+1}}Y'(\alpha\rho_i)Y(\alpha\tilde\rho_i) + Y(\alpha\rho_i)Y'(\alpha\tilde\rho_i)\\
&\quad + W_i^{-1}\sqrt{D_i}\alpha Y'(\alpha\rho_i)Y'(\alpha\tilde\rho_i)\Big],\\
[A_i(\alpha)]_{21} &= Q_i(\alpha)\Big[\sqrt{D_i/D_{i+1}}J'(\alpha\rho_i)J(\alpha\tilde\rho_i) - J(\alpha\rho_i)J'(\alpha\tilde\rho_i)\\
&\quad - W_i^{-1}\sqrt{D_i}\alpha J'(\alpha\rho_i)J'(\alpha\tilde\rho_i)\Big],\\
[A_i(\alpha)]_{22} &= Q_i(\alpha)\Big[\sqrt{D_i/D_{i+1}}Y'(\alpha\rho_i)J(\alpha\tilde\rho_i) - Y(\alpha\rho_i)J'(\alpha\tilde\rho_i)\\
&\quad - W_i^{-1}\sqrt{D_i}\alpha Y'(\alpha\rho_i)J'(\alpha\tilde\rho_i)\Big],
\end{aligned}$$

with

$$Q_i(\alpha) = \frac{1}{J(\alpha\tilde\rho_i)Y'(\alpha\tilde\rho_i) - J'(\alpha\tilde\rho_i)Y(\alpha\tilde\rho_i)}. \tag{13}$$

A repeated application of Eq. (12) allows one to express the coefficients b_i, c_i in terms of b_1, c_1:

$$\begin{pmatrix} b_i\\ c_i\end{pmatrix} = \left[\prod_{j=1}^{i-1}A_j(\alpha)\right]\begin{pmatrix} b_1\\ c_1\end{pmatrix}. \tag{14}$$

The inner boundary condition (6) relates the coefficients b_1 and c_1:

$$\begin{aligned} &b_1(\alpha)\left[\alpha\sqrt{D_1}J'(\alpha\tilde\rho_0) - W_0 J(\alpha\tilde\rho_0)\right]\\ &\quad + c_1(\alpha)\left[\alpha\sqrt{D_1}Y'(\alpha\tilde\rho_0) - W_0 Y(\alpha\tilde\rho_0)\right] = 0, \end{aligned} \tag{15}$$

whose solution is

$$\begin{aligned} b_1(\alpha) &= \alpha\sqrt{D_1}Y'(\alpha\tilde\rho_0) - W_0 Y(\alpha\tilde\rho_0),\\ c_1(\alpha) &= -\alpha\sqrt{D_1}J'(\alpha\tilde\rho_0) + W_0 J(\alpha\tilde\rho_0). \end{aligned} \tag{16}$$

When there is no inner boundary, Eq. (15) is replaced by the condition of regularity of a solution at the origin, yielding $b_1 = 1$ and $c_1 = 0$ (see below). Finally, in the special case of $W_0 = \infty$, Eq. (15) is replaced by $b_1(\alpha)J(\alpha\tilde\rho_0) + c_1(\alpha)Y(\alpha\tilde\rho_0) = 0$, whose solution is

$$\begin{aligned} b_1(\alpha) &= -Y(\alpha\tilde\rho_0),\\ c_1(\alpha) &= J(\alpha\tilde\rho_0). \end{aligned}$$

Eqs. (14) and (16) express all the coefficients b_i and c_i in terms of α. The last unknown parameter, α, can be found from Eq. (5) for the outer boundary condition which implies

$$\begin{aligned} F(\alpha) &= b_\ell(\alpha)\left[\alpha\sqrt{D_\ell}J'(\alpha\rho_\ell) + W_\ell J(\alpha\rho_\ell)\right]\\ &\quad + c_\ell(\alpha)\left[\alpha\sqrt{D_\ell}Y'(\alpha\rho_\ell) + W_\ell Y(\alpha\rho_\ell)\right] = 0. \end{aligned} \tag{17}$$

In the special case of $W_\ell = \infty$, the modified equation is used:

$$F(\alpha) = b_\ell(\alpha)J(\alpha\rho_\ell) + c_\ell(\alpha)Y(\alpha\rho_\ell) = 0.$$

As discussed below, these equations have an infinite set of solutions. Each solution α determines an eigenvalue $\lambda = \alpha^2$, all the coefficients b_i and c_i and thus the radial dependence $v(r)$ of the associated eigenfunction $u(\mathbf{r})$. Consequently, computation of the Laplace operator eigenbasis in multilayered structures is fully reduced to solving Eq. (17). This is a drastic simplification of the problem that allows one to study in depth restricted diffusion in multilayered structures. In what follows, we shall illustrate the use of this equation by several examples.

Since the elements of the matrix $A_i(\alpha)$ contain W_i^{-1}, the permeabilities W_i of the intermediate boundaries should not be *0*. However, if certain W_i was *0*, there would no exchange between the layers i and $i+1$, so that the multilayered structure would be

decomposed into isolated structures. In this case, the computation could be realized for each of these isolated structures separately, while the macroscopic signal would be simply a linear superposition of the signals from each structure. Without loss of generality, one can assume that the permeabilities of the intermediate boundaries are strictly positive. In turn, the permeabilities W_0 and W_ℓ of the inner and outer boundaries can be *0* (reflecting boundary conditions).

2.4. Matrix formalism

The idea of using spectral decompositions for studying restricted diffusion in an inhomogeneous magnetic field goes back to Robertson [30]. A compact matrix representation of the macroscopic signal was progressively developed in a series of publications [31–36,11] (see the review [11] and pedagogical papers [27,28] for a historical survey, comparison between matrix formalisms and technical details). A spectral approach was successfully applied for theoretical and numerical studies of restricted diffusion for various confining domains and magnetic field profiles [37–41]. In this section, we briefly recall the main steps and advantages of the matrix formalism from Refs. [11,27,28].

A solution of the Bloch–Torrey Eq. (1) can be projected onto the complete basis of the Laplace operator eigenfunctions defined through Eqs. (2)–(6). The eigenvalues λ_m, indexed by a positive integer m, are known to be positive, $\lambda_m \geqslant 0$, while the eigenfunctions $u_m(\mathbf{r})$ are orthonormal,

$$\int_\Omega d\mathbf{r}\; u_m^*(\mathbf{r})u_{m'}(\mathbf{r}) = \delta_{m,m'}, \tag{18}$$

where the asterisk denotes the complex conjugate, and $\delta_{m,m'} = 1$ for $m = m'$, and 0 otherwise.

In this basis, the Laplace operator is represented by a diagonal infinite-dimensional matrix Λ formed by the eigenvalues λ_m, $\Lambda_{m,m'} = \delta_{m,m'}\lambda_m$, while the magnetic field in Eq. (1) is represented by another matrix $\mathscr{B}$ whose elements are

$$\mathscr{B}_{m,m'} = \int_\Omega d\mathbf{r}\; u_m^*(\mathbf{r})B(\mathbf{r})u_{m'}(\mathbf{r}).$$

In most practical applications, the magnetic field is induced with a linear gradient in a given direction $\mathbf{e}$ and of strength g so that

$$\mathscr{B}_{m,m'} = \int_\Omega d\mathbf{r}\; u_m^*(\mathbf{r})u_{m'}(\mathbf{r})(\mathbf{e}\cdot\mathbf{r})/L, \tag{19}$$

where $(\mathbf{e}\cdot\mathbf{r})$ is the scalar product between the position $\mathbf{r}$ and the unit vector $\mathbf{e}$ (i.e., the projection of $\mathbf{r}$ onto direction $\mathbf{e}$), and L is a length scale which is introduced to make the matrix $\mathscr{B}$ dimensionless (e.g., L may be the size R of the multilayered structure). In this case, the Larmor frequency is $\omega = \gamma g L$,γ being the gyromagnetic ratio of the nuclei.

The initial magnetization density $\rho(\mathbf{r})$ and the sampling function $\tilde\rho(\mathbf{r})$ of a receiving coil are represented by the infinite-dimensional vectors U and $\widetilde{U}$, respectively:

$$U_m = Vol^{1/2}\int_\Omega d\mathbf{r}\; u_m^*(\mathbf{r})\rho(\mathbf{r}),$$
$$\widetilde{U}_m = Vol^{-1/2}\int_\Omega d\mathbf{r}\; u_m(\mathbf{r})\tilde\rho(\mathbf{r}),$$

Vol being the volume of the multilayered structure Ω. In practice, both functions $\rho(\mathbf{r})$ and $\tilde\rho(\mathbf{r})$ are often constant, $\rho(\mathbf{r}) = 1/Vol$ and $\tilde\rho(\mathbf{r}) = 1$ so that

$$U_m = \widetilde{U}_m^* = Vol^{-1/2}\int_\Omega d\mathbf{r}\; u_m^*(\mathbf{r}). \tag{20}$$

The macroscopic signal acquired at observation time t is proportional to the integral of the magnetization $m(\mathbf{r},t)$, multiplied by the sampling function $\tilde\rho(\mathbf{r})$, over the confining domain Ω. When the magnetic field does not vary in time ($f(t) = 1$), the signal attenuation (i.e., the signal normalized by the reference signal without magnetic field) can be written in a compact matrix form of a scalar product [11,27,28]

$$E = \left(U\exp[-(\Lambda + i\omega\mathscr{B} + \mathscr{B}^{\mathrm{r}})t]\widetilde{U}\right), \tag{21}$$

where the matrix $\mathscr{B}^{\mathrm{r}}$ accounts for bulk relaxation in different layers:

$$\mathscr{B}^{\mathrm{r}} = \sum_{i=1}^{\ell} T_i^{-1}\mathscr{B}^{\mathrm{i}}, \quad \mathscr{B}^{\mathrm{i}}_{m,m'} = \int_{\Omega_i} d\mathbf{r}\; u_m^*(\mathbf{r})u_{m'}(\mathbf{r}). \tag{22}$$

If the temporal profile $f(t)$ of the magnetic field is a piecewise constant function, i.e., $f(t) = f_k$ on (t_{k-1},t_k), $k = 1\ldots K$, with $t_0 = 0$ and $t_K = t$, the signal attenuation is combined from the evolution matrices for each time interval (t_{k-1}, t_k),

$$E = \left(U\left[\prod_{k=1}^{K}\exp\left[-(\Lambda + i\omega f_k\mathscr{B} + \mathscr{B}^{\mathrm{r}})(t_k - t_{k-1})\right]\right]\widetilde{U}\right). \tag{23}$$

This formula is exact, no approximation was used. For instance, the signal attenuation in a rectangular bipolar gradient profile shown in Fig. 2 (with $t_1 = 0$ and $\tau = \Delta = t/2$) is

$$E = \left(U\left[e^{-(\Lambda+i\omega\mathscr{B}+\mathscr{B}^{\mathrm{r}})\delta}e^{-(\Lambda+\mathscr{B}^{\mathrm{r}})(t/2-\delta)}e^{-(\Lambda-i\omega\mathscr{B}+\mathscr{B}^{\mathrm{r}})\delta}e^{-(\Lambda+\mathscr{B}^{\mathrm{r}})(t/2-\delta)}\right]\widetilde{U}\right). \tag{24}$$

Since any temporal profile $f(t)$ can be approximated by a piecewise constant function, the matrix formalism allows one to compute the signal in a very general situation.

For a numerical implementation, the infinite-dimensional matrices and vectors have to be truncated to a finite size M. For this purpose, the eigenvalues λ_m are sorted in an ascending order, and one chooses the first M eigenvalues and the corresponding eigenfunctions. A numerical algorithm consists in the following steps:

(1) compute the first M eigenvalues and corresponding eigenfunctions of the Laplace operator in a given confining domain;
(2) construct the matrices $\mathscr{B}$ and $\mathscr{B}^{\mathrm{r}}$ and the vectors U and $\widetilde{U}$ for given magnetic field $B(\mathbf{r})$, initial density $\rho(\mathbf{r})$ and sampling function $\tilde\rho(\mathbf{r})$; and
(3) approximate a given temporal profile $f(t)$ and compute the signal attenuation by matrix multiplication in Eq. (23).

For a general confining domain, a numerical computation of the Laplace operator eigenfunctions is often the most time-consuming step. In turn, the first step of the algorithm is skipped

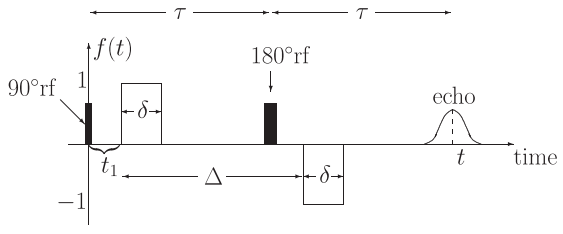

Fig. 2. Example of an effective temporal profile $f(t)$: two rectangular gradient pulses of duration δ separated by the period Δ. The second gradient pulse has the opposite sign due to the inverting 180° rf pulse. The total echo time is $t = 2\tau$, and t_1 is the delay between the 90° rf pulse and the first gradient pulse. Throughtout the paper, we set $t_1 = 0$ and $\tau = \Delta = t/2$ in order to avoid confusion with notation for the Laplace operator, although different values for τ and Δ can be directly used in the matrix formalism.

for multilayered structures, because the eigenfunctions are already known. The main contribution of the paper is the derivation of the explicit analytical formulas for the elements of the matrices $\mathscr{B}, \mathscr{B}^{\mathrm{r}}$ and the vectors $U, \widetilde{U}$. These formulas help to perform the second step of the algorithm in a very efficient way. In addition, analytical results eliminate numerical integrations which otherwise could degrade the accuracy of computation. Thanks to the explicit formulas, numerical errors which come only from matrix truncation and matrix products, can be made negligibly small. Finally, an explicit construction of these matrices is very rapid (see Appendix B for an explicit example of the matrices Λ and $\mathscr{B}$). In summary, analytical computation of the governing matrices for multilayered structures makes the matrix formalism to be efficient, rapid and accurate numerical method which outperforms classical techniques such as Monte Carlo simulations or finite difference and finite element resolution of the Bloch–Torrey equation.

2.5. Three types of multilayered structures

2.5.1. Slab layers

Diffusion in a slab between two parallel planes is decomposed in two independent processes, one is orthogonal and the other is parallel to the planes. Since the latter is not restricted, the signal attenuation due to this process is well known [42,43]. One can therefore focus on the orthogonal one-dimensional diffusion which is mathematically equivalent to diffusion on the interval $\Omega = [r_0,R]$. In this case, there is no angular part ($\nu = 0$) and the "radial" eigenvalue Eq. (9) is simply $v'' + \nu = 0$. Two independent solutions of this equation are

$$J(z) = \cos(z), \quad Y(z) = \sin(z),$$

so that $Q_i(\alpha) = 1$ according to Eq. (13).

When $r_0 = 0$, Eq. (16) yields $b_1(\alpha) = \alpha\sqrt{D_1}$ and $c_1(\alpha) = W_0$ for any permeability $W_0 < \infty$. In the special case of a perfectly absorbing inner boundary ($W_0 = \infty$), Eq. (16) are not valid, and one can use $b_1 = 0$ and $c_1 = 1$.

For the simplest case of a single layer with reflecting boundaries at $r = 0$ ($W_0 = 0$) and $r = R$ ($W_1 = 0$), Eq. (17) is reduced to $F(\alpha) = -\alpha^2 D_1 \sin(\alpha\rho_1) = 0$, which has an infinite set of positive roots $\pi k/\rho_1$, with k ranging from 0 to infinity. The eigenvalues and eigenfunctions are $\pi^2 k^2 D_1/R^2$ and $\cos(\pi k\, r/R)$, as expected for the interval with reflecting endpoints.

A general situation is somewhat similar to the above example. In fact, Eq. (17) has an infinite set of the positive roots which can be denoted as α_{0k}, with k ranging from 0 to infinity (we write the index $0k$ instead of k for convenience, see below). These roots determine the eigenvalues $\lambda_{0k} = \alpha_{0k}^2$ and the eigenfunctions $u_{0k}(r)$ of the Laplace operator

$$u_{0k}(r) = \sqrt{\frac{2}{R - r_0}}\beta_{0k} v_{0k}(r),$$

where the normalization constants β_{0k} are set to fulfill Eq. (18), i.e.

$$1 = \int_{r_0}^{R} dr\; u_{0k}^2(r) = 2\beta_{0k}^2 \frac{1}{R - r_0}\int_{r_0}^{R} dr\, v_{0k}^2(r).$$

The elements of the vector U and of the matrices $\mathscr{B}, \mathscr{B}^{\mathrm{r}}$ from Eqs. (20), (19), (22) are expressed in terms of several integrals which are given explicitly in Appendix A:

$$\begin{aligned} &\beta_{0k} = (2I_{0k})^{-1/2},\\ &U_{0k} = \sqrt{2}\beta_{0k} J_k,\\ &\mathscr{B}^i_{0k,0k'} = 2\beta_{0k}\beta_{0k'} I_{0kk',i},\\ &\mathscr{B}_{0k,0k'} = 2\beta_{0k}\beta_{0k'} K_{0k,0k'}. \end{aligned} \tag{25}$$

All the quantities $I_{0k}, J_k, I_{nkk',i}$ and $K_{0k,0k'}$ are fully and explicitly expressed in terms of the positive roots α_{0k} of Eq. (17). A numerical computation is therefore reduced to finding these roots and applying explicit formulas to construct the matrices $\mathscr{B}, \mathscr{B}^{\mathrm{r}}$ and the vector U. Practical applications of the matrix formalism will be illustrated in Section 3.

2.5.2. Cylindrical layers

A diffusive process inside a cylinder has two independent components: one-dimensional unrestricted diffusion along the cylinder axis and two-dimensional restricted diffusion in the perpendicular plane. The latter is mathematically equivalent to restricted diffusion in a disk. In this case, $\Delta_{\mathrm{ang}} = \partial^2/\partial\theta^2$, and Eq. (8) has infinitely many solutions $e^{in\theta}$ and $e^{-in\theta}$, indexed by an integer $n = 0,1,2,\ldots$, with $\nu_n = n^2$. The radial eigenvalue Eq. (9) is the Bessel equation with two independent solutions

$$J(z) = J_n(z), \quad Y(z) = Y_n(z),$$

which are Bessel functions of the first and second kind. The function $Q_i(\alpha)$ in Eq. (13) is $Q_i(\alpha) = \pi\alpha\tilde{\rho}_i/2$ according to the Abel's identity:

$$J_n(z)Y_n'(z) - Y_n(z)J_n'(z) = \frac{2}{\pi z}.$$

If $r_0 = 0$, there is no inner boundary, and Eq. (15) is replaced by the condition of regularity of a solution at the origin. Given that Bessel functions $Y_n(z)$ diverge at $z = 0$, one imposes $c_1 = 0$, while b_1 can be set to 1.

For any fixed n, Eq. (17) has an infinite set of positive solutions which can be denoted as α_{nk} ($k = 0,1,2,\ldots$). The double index nk is used instead of the single index m for convenience. The solutions α_{nk} determine the eigenvalues $\lambda_{nk} = \alpha_{nk}^2$ and the eigenfunctions $u_{nk}(r,\theta)$ of the Laplace operator:

$$u_{nk}(r,\theta) = \frac{\varepsilon_n \beta_{nk}}{\sqrt{\pi(R^2 - r_0^2)}} v_{nk}(r)\cos n\theta,$$

where $\varepsilon_n = \sqrt{2}$ for $n > 0$, and $\varepsilon_0 = 1$. The normalization constants β_{nk} are set to fulfill Eq. (18). The explicit formulas from Appendix A yield

$$\begin{aligned} &\beta_{nk} = (2I_{nk})^{-1/2},\\ &U_{nk} = 2\delta_{n,0}\beta_{0k} J_k,\\ &\mathscr{B}^i_{nk,n'k'} = 2\delta_{n,n'}\beta_{nk}\beta_{nk'} I_{nkk',i},\\ &\mathscr{B}_{nk,n'k'} = \delta_{n,n'\pm1}(1 + \delta_{n,0} + \delta_{n',0})^{1/2}\beta_{nk}\beta_{n'k'} K_{nk,n'k'}. \end{aligned} \tag{26}$$

Since all these quantities are explicitly expressed in terms of α_{nk}, computation is reduced to finding the positive roots of Eq. (17). It is worth stressing again that the elements of the matrices $\mathscr{B}, \mathscr{B}^i$ are indexed by two double indices nk and $n'k'$ (e.g., $\mathscr{B}_{nk,n'k'}$ is a matrix, not a tensor of the fourth rank).

2.5.3. Spherical layers

In three dimensions, the eigenfunctions of the "angular" Laplace–Beltrami operator Δ_{ang} are the spherical harmonics, with the associate eigenvalues $\nu_n = n(n+1)$ ($n = 0,1,2,\ldots$). Eq. (9) has two independent solutions known as spherical Bessel functions of the first and second kind,

$$J(z) = j_n(z), \quad Y(z) = y_n(z),$$

where $j_n(z) = \sqrt{\pi/(2z)}J_{n+1/2}(z)$ and $y_n(z) = \sqrt{\pi/(2z)}Y_{n+1/2}(z)$. The Abel's identity

$$j_n(z)y_n'(z) - y_n(z)j_n'(z) = \frac{1}{z^2}$$

yields $Q_i(\alpha) = \alpha^2\tilde{\rho}_i^2$ in Eq. (13).

If $r_0 = 0$, there is no inner boundary, and Eq. (15) is replaced by the condition of regularity of a solution at the origin. Given that spherical Bessel functions $y_n(z)$ diverge at $z = 0$, one imposes $c_1 = 0$, while b_1 can be set to 1.

As in the case of cylindrical layers, Eq. (17) has an infinite set of positive solutions denoted as α_{nk} ($k = 0,1,2,\ldots$). The eigenvalues $\lambda_{nk} = \alpha_{nk}^2$ and the eigenfunctions are

$$u_{nk}(r,\theta,\varphi) = \frac{\beta_{nk}\sqrt{2n+1}}{\sqrt{2\pi(R^3 - r_0^3)}}\, v_{nk}(r) P_n(\cos\theta) e^{il\varphi}, \tag{27}$$

where $P_n(z)$ is the Legendre polynomial. Since the magnetic field is independent of the angular variable φ, the third index l is omitted. The normalization constants β_{nk} are set to fulfill Eq. (18). The explicit formulas from Appendix A yield

$$\begin{aligned} \beta_{nk} &= (2I_{nk})^{-1/2}, \\ U_{nk} &= \delta_{n,0}\sqrt{6}\beta_{0k} J_k, \\ \mathscr{B}^i_{nk,n'k'} &= 2\delta_{n,n'}\beta_{nk}\beta_{nk'} I_{nkk',i}, \\ \mathscr{B}_{nk,n'k'} &= \delta_{n,n'\pm 1}\frac{n+n'+1}{\sqrt{(2n+1)(2n'+1)}}\beta_{nk}\beta_{n'k'} K_{nk,n'k'}. \end{aligned} \tag{28}$$

2.6. Practical implementation

Explicit formulas for the elements of the governing matrices $\mathcal{A}$, $\mathscr{B}$, and $\mathscr{B}^i$ are the key point for efficient numerical computation. An *a priori* sophisticated computation of the signal attenuation due to magnetic field encoding, relaxation and diffusion in multilayered structures is reduced to finding roots of explicit functions in Eq. (17). Once these roots are found numerically, the construction of the governing matrices and the computation of the signal attenuation are straightforward.

2.6.1. Finding roots

Although finding roots of explicit functions is a classical problem in numerical analysis, several comments are in order. Since the governing matrices have to be truncated to a finite size, it is convenient to set the upper limit $\alpha_{\max}$ and to search for all the roots of Eq. (17) in the interval $(0,\alpha_{\max})$. An appropriate choice for $\alpha_{\max}$ (or the truncation size) will be discussed in the next subsection. In two and three dimensions, the roots of Eq. (17) should be found for different values of the index $n = 0,1,2,\ldots$. Since the smallest strictly positive root α_{n0} of Eq. (17) increases with n, the searching procedure is stopped at some $n_{\max}$ for which Eq. (17) does not have roots on the interval $(0, \alpha_{\max})$.

The main numerical difficulty is that the number of roots on the interval $(0, \alpha_{\max})$, as well as the distances between roots, are unknown. Classical methods (e.g., the bisection method) can find a *single* root on some interval $[a,b] \subset (0,\alpha_{\max})$. How can one choose the interval $[a,b]$ so that it contains at most one root? For a single-layer structure, the answer is simple. For instance, in the case of the unit disk with Neumann boundary condition, Eq. (17) is reduced to $F(\alpha) = \alpha^2 D_1 J_n'(\alpha) = 0$, and the distance between any two roots of this equation is greater than 1. One can therefore split the interval $(0,\alpha_{\max})$ in subintervals (0,1), (1,2),... so that each of them contains at most one root. Searching for roots on each subinterval by classical methods yields all the roots on the interval $(0,\alpha_{\max})$.

In the general case, however, the computation is more difficult because two roots of Eq. (17) can be close to each other, and the minimal distance between roots depends on the physical parameters. This difficulty is illustrated on Fig. 3 which shows the function $F(\alpha)$ from Eq. (17) for two adjacent intervals of length r, with

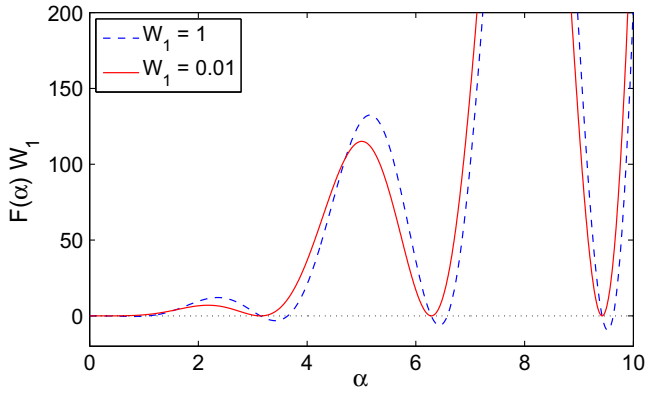

Fig. 3. Function $F(\alpha)$ from Eq. (29) for two unit intervals with $D_1 = D_2 = 1$ (a.u.), $W_0 = W_2 = 0$, and two values $W_1 = 1$ (a.u.) and $W_1 = 0.01$ (a.u.), shown by blue dashed line and red solid line, respectively. The roots form pairs, and the distance between two roots in each pair decreases when W_1 is decreased.

$D_1 = D_2 = D$, and $W_0 = W_2 = 0$ (Neumann boundary condition at both endpoints):

$$F(\alpha) = \frac{\alpha^3 D^{3/2}}{W_1}\left[\sin^2(\alpha r/\sqrt{D}) - W_1\frac{\sin(2\alpha r/\sqrt{D})}{\alpha\sqrt{D}}\right]. \tag{29}$$

When the permeability W_1 between two intervals approaches 0, the second term vanishes, and the positive roots of the function $F(\alpha)$ approach $\pi k\sqrt{D}/r$ ($k = 0,1,2,\ldots$), as in the case of two disconnected intervals of length r. A numerical computation of these roots is in general a difficult task.

In practice, the roots of $F(\alpha)$ can be found in the same way as for the unit disk, namely, by splitting the interval $(0,\alpha_{\max})$ into many small subintervals: $(0, \varepsilon)$, $(\varepsilon, 2\varepsilon)$, etc. On one hand, the length ε should be small enough to ensure that each subinterval contains no more than one root. On the other hand, larger ε leads to faster computation. The simplest practical scheme for choosing the length ε is a visual estimation of ε by plotting the function $F(\alpha)$ and looking at the minimal distance between its roots. An algorithm for an automated choice of the optimal length ε is in progress and will be published elsewhere.

2.6.2. Choice of numerical parameters

The choice of numerical parameters is a compromise between accuracy and rapidity of the algorithm. The central numerical parameter of the matrix formalism is the truncation size M of the governing matrices or, equivalently, the upper limit $\alpha_{\max}$. In mathematical terms, the truncation is accurate when the matrices $\mathscr{B}$ and $\mathscr{B}^r$ in Eq. (21), representing "perturbations" of the Laplace operator in the Bloch–Torrey equation, are "small" in comparison to the matrix $\mathcal{A}$. In particular, stronger gradients (larger ω) would require larger matrices. For simple domains (e.g., the unit sphere), matrices of size 10×10 or 20×20 are often enough for accurate computations (see Appendix B). In multilayered structures, the presence of various time and length scales may require larger matrices. For all the computations in this paper, the truncation to the size 100×100 was enough to get very accurate results. Although it is difficult to provide a general criterion for the truncation size, a simple rule-of-thumb can be suggested. As the macroscopic signal must not depend on the choice of numerical parameters, one can check whether two signals computed with the matrices of different truncation sizes are close enough.

In order to illustrate the rapidity and accuracy of the matrix formalism, we consider restricted diffusion in a cylindrical bilayer structure, with $r_1 = 2.5$ μm, $r_2 = 5$ μm, $D_1 = 2 \cdot 10^{-10}$ m^2/s, $D_2 = 2 \cdot 10^{-9}$ m^2/s, $W_0 = W_2 = 0$, $W_1 = 10^{-5}$ m/s, $t = 100$ ms and

$g = 200$ mT/m (the choice of these values will be explained in Section 3). The signal attenuation was computed in MATLAB on a home laptop (Intel Core Duo at 2.5 GHz, RAM 4 GB, a 32 bit operating system) using the matrices with different truncation sizes M. The computation with $M = 200$ was considered as the "exact" reference, to which the computations with M varying from 10 to 100 were compared with. The following empirical relations were found: $\mathrm{Err} \sim 0.68M^{-2.81}$, $T_M \sim 4.5 \cdot 10^{-3}M^{1.5}$ and $T_S \sim 4.6 \cdot 10^{-7}M^{2.73}$, where Err is the relative error between the approximate and reference signals, T_M is the CPU time (in seconds) for constructing all governing matrices, and T_S is the CPU time (in seconds) for computing the signal attenuation. Even for the truncation size $M = 10$, the relative error is less than 0.1% (which is comparable to the best available experimental accuracy), while its computation requires less than one second of CPU time on a home laptop. Such performances are unattainable for classical numerical techniques. It is worth stressing however, that these performances strongly depend on the problem at hand so that the above empirical relations may change for other examples. For instance, computations for one-dimensional systems are much faster. In turn, the presence of many layers would slow down the computation, while small permeabilities or large differences in diffusion coefficients would require larger matrices.

3. Numerical results

For illustrative purposes, the spin-echo signal attenuation was computed for several examples by using the matrix formalism and sometimes by Monte Carlo simulations. The following typical values for physical parameters were used: $D = 2 \cdot 10^{-9}$ m^2/s for the free diffusion coefficient of water molecules at ambient temperature, $R = 5$ μm as the outer radius, and $\gamma = 2.675 \cdot 10^8$ rad T^{-1} s^{-1} for the gyromagnetic ratio of protons. The gradient intensity g and observation time t were varied in large ranges. The corresponding b-value of the bipolar gradient profile (shown in Fig. 2) was $b = \gamma^2 g^2 \delta^2 (t/2 - \delta/3)$. The focus was on cylindrical bilayer structures with Neumann boundary condition at the outer boundary.

3.1. The role of the intermediate permeability

The role of permeable boundaries in diffusion-weighted experiments was studied by many authors [44–54]. In their seminal paper, Brownstein and Tarr used the spectral approach in order to investigate the signal attenuation due restricted diffusion inside a sphere subject to surface relaxation, which is also equivalent to one-way permeation of the spin-bearing particles outside the sphere [44]. Tanner considered diffusion between parallel semi-permeable barriers and revealed the dependence of the time-dependent diffusion coefficient on the permeability [45]. Andrasko and later Kuchel et al. measured the water permeability of human erythrocytes by using a PGSE technique [46,47]. Barzykin et al. studied two-way diffusive exchange between a sphere and an outer space [48,49]. In the framework of the narrow-pulse approximation (see Section 3.4), Kuchel and Durrant considered restricted diffusion inside two and four slabs separately by permeable membranes [50]. A simplified pore-to-pore hopping model for the two-phase diffusion problem was developed by Jiang et al. for the analysis of the pulsed-gradient spin-echo (PGSE) attenuation of water diffusion in the condensed cell suspension systems [51]. In this model, the two phases inside and outside the cells are treated as two different kinds of pores, and the spin-bearing molecules perform hopping diffusion between them. Sen derived corrections due to permeability to the time-dependent diffusion coefficient in the short-time limit [52,53]. Kezele et al. examined the signal attenuation in spherical cells with semi-permeable cellular and nuclear membranes [54]. They built an analytic model that could explain cell characteristic sizes, including the nuclear size, as well as the cell-membrane permeability, the features that are suggested to be related to different tissue pathologies.

In order to illustrate the use of the matrix formalism, we consider a bilayer cylindrical structure of radii $r_1 = R/2$ and $r_2 = R$, with equal diffusion coefficients $D_1 = D_2 = D$, $t = 100$ ms, $\delta = t/2$ and three values of the permeability W_1 of the intermediate boundary: $W_1 = \infty$ (fully permeable boundary), $W_1 = 10^{-5}$ m/s (typical water permeability for axons [19,20]), and $W_1 = 10^{-7}$ m/s (almost impermeable boundary). The gradient strength g was varied between 0 and 200 mT/m.

The diffusion length $\sqrt{Dt} \approx 14$ μm is much larger than the size of the bilayer system meaning the long-time or motional averaging regime [11]. In this regime, the Gaussian phase approximation is expected to be applicable, and the signal would decay exponentially with the b-value, $E(b) \approx \exp[-\mathrm{ADC}\, b]$. At the same time, the signal attenuation in the long-time regime is described as

$$E \approx \exp\left[-\zeta_{-1}\frac{\gamma^2 g^2 L^4}{D}\int_0^t dt' f^2(t')\right], \tag{30}$$

where L is the size of the system, and ζ_{-1} is the geometry-dependent constant [11]. For a cylinder of radius L, Neuman found this constant to be 7/96 (there is a misprint in Neuman's paper: his constant 7/296 should read as 7/96) [55]. For the bipolar gradient profile shown on Fig. 2, one has $b = \gamma^2 g^2 \delta^2 (t/2 - \delta/3)$ and the integral in Eq. (30) is simply 2δ so that the apparent diffusion coefficient (ADC) can be approximated as

$$\mathrm{ADC} \approx \frac{2\zeta_{-1}L^4}{D\delta(t/2 - \delta/3)}. \tag{31}$$

For the infinite permeability W_1, the bilayer system is simply a cylinder of radius $L = R$, for which $\mathrm{ADC} \approx 2.7 \cdot 10^{-11}$ m^2/s according to Eq. (31). The signal attenuation is indeed exponential, as illustrated on Fig. 4 by blue[1] dashed line.

In the opposite limit of zero (or very small) permeability W_1, the bilayer system is decomposed in two isolated subdomains: a cylinder of radius $R/2$ and a cylindrical shell of radii $R/2$ and R. As previously, the monoexponential signal attenuations E_i and E_o are expected for both subdomains, as shown by two black dotted lines on Fig. 4. The corresponding ADCs are $1.7 \cdot 10^{-12}$ m^2/s and $5 \cdot 10^{-11}$ m^2/s (the second value is less accurate because it is extracted from fitting $-\log(E(b))$ for small b). The signal attenuation from such bilayer system is a weighted combination (shown by circles) of the two signal attenuations:

$$E = (1/4)E_i + (3/4)E_o,$$

where the weights 1/4 and 3/4 are volume fractions of the inner cylinder and the outer cylindrical shell, respectively. The signal attenuation E as a function of b exhibits thus a bi-exponential decay, with two different ADCs, in spite of the fact that water in both compartments has the same diffusion coefficient D. In other words, the smallness of both ADCs in comparison to D does not necessarily mean a reduction of the microscopic mobility of water molecules. It is uniquely a reflection of compartmentation. This example illustrates potential ambiguities of ADCs whose interpretation may be strongly misleading, as it was already stressed [20,56]. When the intermediate permeability is very small ($W_1 = 10^{-7}$ m/s), the signal attenuation, shown by green dash-dotted line, is close to the limiting case of $W_1 = 0$.

[1] For interpretation of color in Figs. 3–8, the reader is referred to the web version of this article.

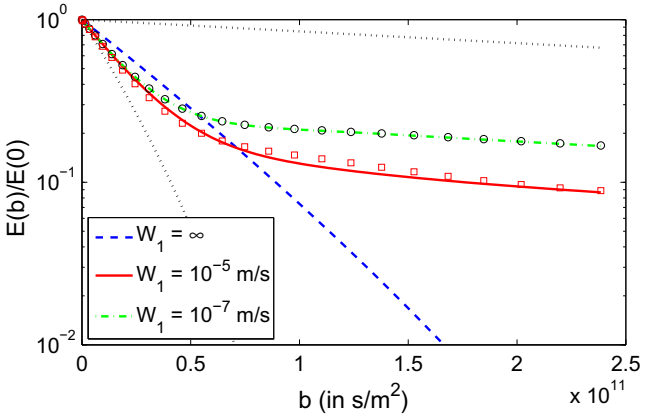

Fig. 4. Signal attenuation as a function of the b-value for restricted water diffusion in cylindrical bilayer system, with $r_1 = 2.5$ μm, $r_2 = 5$ μm, $D_1 = D_2 = 2 \cdot 10^{-9}$ m^2/s, $t = 100$ ms, $\delta = 50$ ms, $g = 0 - 200$ mT/m. Dashed, solid and dash-dotted lines show the signal attenuation for three values of the permeability W_1 (infinity, 10^{-5} m/s and 10^{-7} m/s, respectively). Two black dotted lines indicate the signal attenuation E_i for the isolated cylinder of radius r_1 and the signal attenuation E_o for the isolated cylindrical shell of radii r_1 and r_2 (the latter curve decays much faster). As expected, these two signals as functions of b exhibit monoexponential decay. Circles show the weighted sum $(1/4)E_i + (3/4)E_o$ which corresponds to the bilayer system with zero permeability. Squares indicate the signal attenuation for $W_1 = 10^{-5}$ m/s computed by Monte Carlo simulations.

The curve shown by red solid line corresponds to typical water permeability in axons, $W_1 = 10^{-5}$ m/s. Although this curve can also be fitted as bi-exponential, the corresponding ADCs are affected by the permeability. This feature should be taken into account for a reliable interpretation of experimental data. In order to check the validity of the matrix formalism, the signal attenuation was also computed by Monte Carlo simulations. Since a classical scheme was employed (see, e.g., [57]), its full description is omitted. We only note that the finite permeability was implemented as a random choice for reflection or transfer across the boundary, the reflection probability being related to the permeability, diffusion coefficient and discretization step [58]. Fig. 4 shows that the matrix formalism and Monte Carlo simulations give similar results.

3.2. Different diffusion coefficients

As the second example, we consider a cylindrical bilayer system with different diffusion coefficients D_1 and D_2, each of them is equal either to D (free diffusion coefficient of water), or to $D/10$ (strongly hindered diffusion coefficient for water in gel or crowded environment). The other physical parameters remain the same as in the previous subsection. Both diffusion lengths, 14 μm and 4.5 μm (for D and $D/10$, respectively) are larger than, or comparable to, the compartment sizes.

For simple confining shapes, an increase of the diffusion coefficient leads to a weaker signal decay (i.e., a smaller ADC according to Eq. (31)). This is a counter-intuitive feature of the motional averaging or long-time regime [11]. During a long diffusive exploration, the nuclei visit various regions of the confining domain and thus experience almost all possible values of the gradient, and this motional averaging being stronger for larger diffusion coefficients. Spatial heterogeneities of the magnetic field are therefore partly averaged, and the signal is less attenuated. This behavior is clearly seen on Fig. 5a in which the spin-echo signal attenuation is plotted as a function of b for the isolated inner cylinder of radius $r_1 = R/2 = 2.5$ μm. In turn, the behavior of the spin-echo signal attenuation for the isolated outer cylindrical shell is different. On Fig. 5b, the signal is stronger attenuated for larger diffusion coefficient. This discrepancy can be explained by the fact that the nuclei traveling along the circumferences of the cylindrical shell explore distances in the order of $15 - 30$ μm, and the long-time regime is not yet established. The signal behavior in single circular and spherical layers was thoroughly investigated in [39].

As expected, the signal attenuation in the whole multilayered structure exhibits a complicated dependence on the gradient strength and diffusion coefficient. Fig. 6 shows the signal attenuation for four combinations of the diffusion coefficients D_1 and D_2, when the intermediate boundary is impermeable ($W_1 = 0$), partially permeable ($W_1 = 10^{-5}$ m/s), and fully permeable ($W_1 = \infty$). In the former case, $E = (1/4)E_i + (3/4)E_o$, and the behavior of the signal attenuations E_i and E_o in the two isolated compartments suggest to expect the strongest signal attenuation for $D_1 = D/10$ and $D_2 = D$ (green dashed curve), while the weakest signal attenuation is expected for $D_1 = D$ and $D_2 = D/10$ (red dash-dotted line). Two other combinations, $D_1 = D_2 = D$ and $D_1 = D_2 = D/10$, yield intermediate signal attenuations. This example illustrates how sophisticated the behavior of the signal may be, even in the simplest multilayered structure with no permeability. Further theoretical analysis of the signal attenuation is necessary for a reliable fitting and interpretation of experimental data.

For a typical value of water permeability in cells and axons ($W_1 = 10^{-5}$ m/s), the signal behavior is similar to that for impermeable boundary. For this example, the permeability may be neglected in order to lighten the analysis and fitting procedures. However, the diffusive exchange through the intermediate boundary may become crucial for other choices of physical parameters, i.e., permeability, compartments sizes, diffusion coefficients,

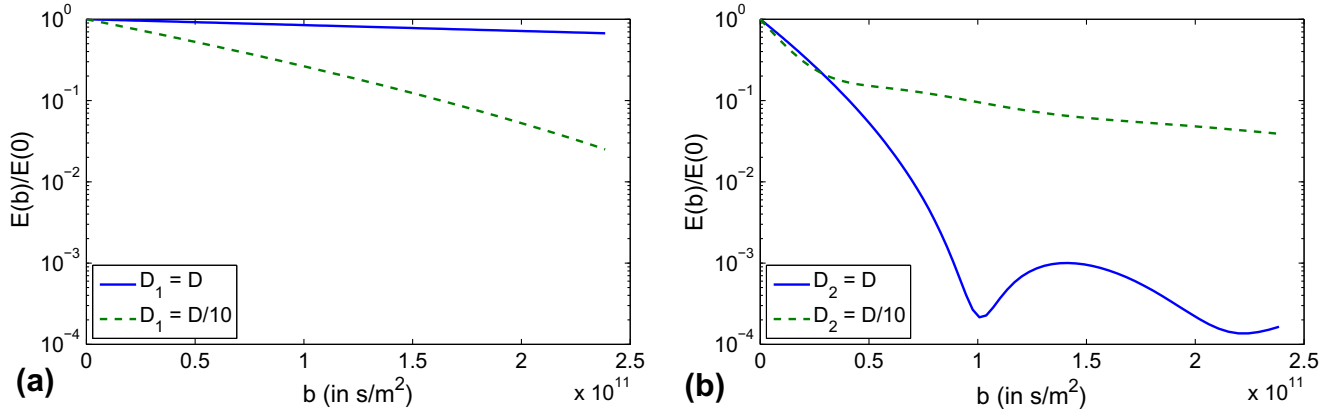

Fig. 5. Signal attenuation in two isolated compartments of the bilayer system: (a) the inner cylinder and (b) the outer cylindrical shell.

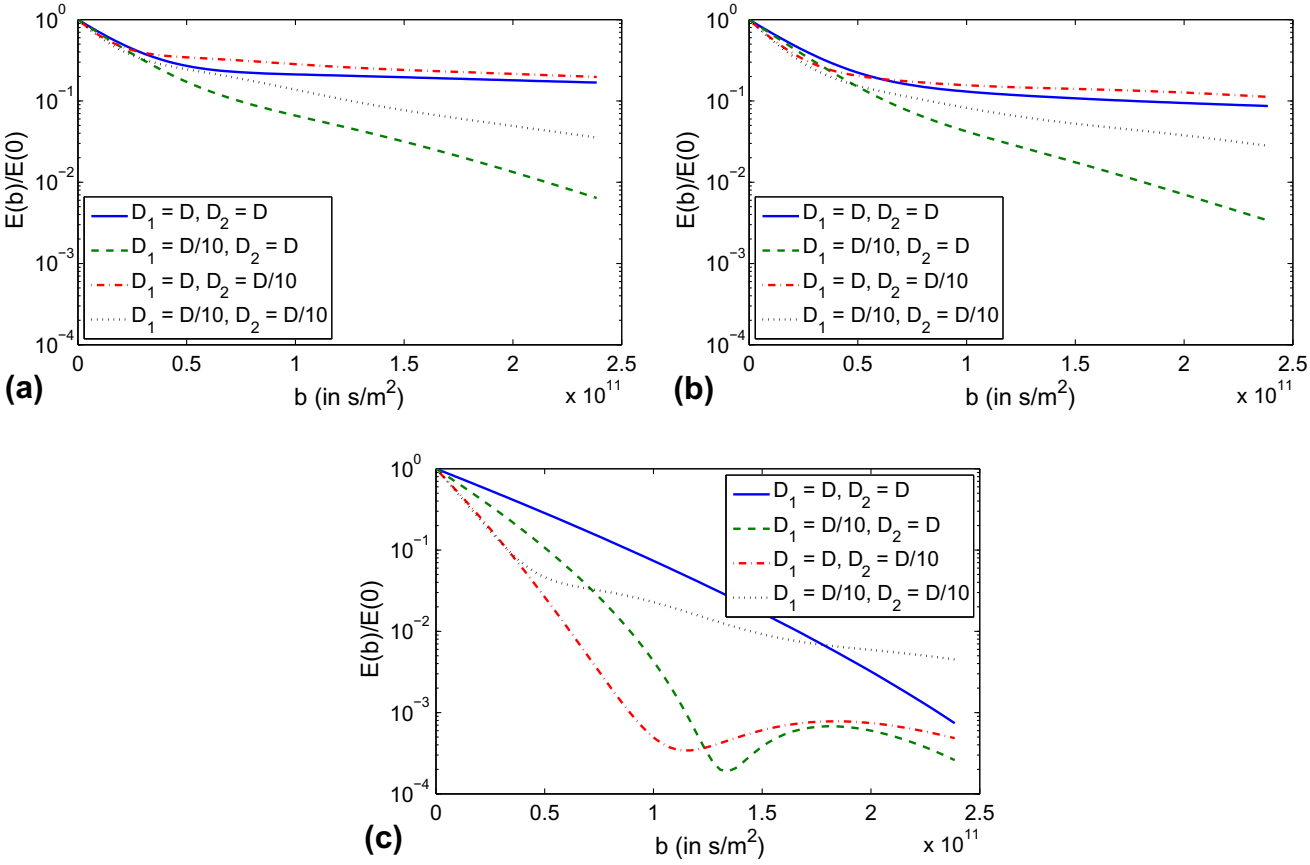

Fig. 6. Signal attenuation in the cylindrical bilayer system with four combinations of diffusion coefficients D_1 and D_2, when the intermediate boundary is impermeable ($W_1 = 0$, a), partially permeable ($W_1 = 10^{-5}$ m/s, b), and fully permeable ($W_1 = \infty$, c).

observation time, etc. Using the matrix formalism, one can accurately determine whether this exchange is relevant or not for a given set of parameters.

When the permeability W_1 is infinite, the behavior of the signal is different. For instance, the case $D_1 = D$ and $D_2 = D/10$ (red dash-dotted line) which exhibited the weakest signal attenuation for impermeable boundary, leads to the strongest attenuation for a fully permeable boundary. Diffraction-like patterns [59] start to appear for other cases. A detailed study of the signal behavior in multilayered structures will be published elsewhere.

3.3. Modeling the extracellular space

A multilayered structure is often a part of a larger medium. For instance, living cells or axons are immersed in the surrounding extracellular space which can be considered as an infinite medium as compared to the size of the multilayered structure. Water molecules or other species can diffuse across the outer boundary of the multilayered structure into the extracellular space and back.

In a first approximation, the diffusive exchange with the extracellular space is implemented in Eq. (1) through the permeability W_ℓ of the outer boundary. This implementation assumes a one-way exchange, namely, permeation from the multilayered structure to the extracellular space. In other words, any particle may leave the multilayered structure, but no particle can enter (or return) inside it. This assumption can in principle be realized in experiments in which the extracellular space is filled with strong relaxation agents (e.g., Mn^{2+} ions). These agents are supposed to ensure infinitely fast relaxation in the extracellular space so that once a particle leaves the multilayered structure, its magnetization is immediately destroyed. When two-way exchange is expected, more elaborate models are needed.

A rigorous "connection" between the multilayered structure and an infinite surrounding medium is a tedious task. In fact, if a spectral approach was employed, the main difficulty would be the emergence of a continuous part of the Laplace operator spectrum for the infinite medium. This problem was partly solved by Barzykin et al. for a sphere immersed in the extracellular space [48]. Using the narrow-pulse approximation, they computed the signal attenuation in the long-time regime when the continuous part of the spectrum can be neglected.

We propose another, more physics-oriented approach. In MRI experiments, the excitation of the nuclei and the signal acquisition are performed inside a voxel which often englobes a biological system (e.g., a living cell) and a part of the surrounding extracellular space. For the sake of simplicity, we assume that the voxel has a rotation-invariant shape of radius R (in principle, any voxel shape could be implemented, although the computation would be more sophisticated). The nuclei, which were excited inside the voxel, can leave it and possibly return before the observation time. What is an appropriate boundary condition at the edge of the voxel? Neumann boundary condition would prohibit the nuclei to leave the voxel, while Dirichlet boundary condition does not allow them to return. An intermediate Robin boundary condition might work, although there is no physical frontier around the voxel, and the choice of the permeability at this fictitious frontier is problematic. To overcome this difficulty, we propose to introduce a supplementary layer around the voxel. The width of this layer can be chosen to be around $2\sqrt{Dt}$, D being the water diffusion coefficient in the extracellular space. In this case, the water molecules which left

the voxel, do not have enough time to cross the supplementary layer and to arrive towards its boundary. As a consequence, the presence of this fictitious boundary and its boundary condition do not influence the signal attenuation.

In order to clarify this idea, we consider a spherical cell of radius $r_1 = 1$ μm immersed in the extracellular space. For our illustrative purposes, the diffusion coefficients inside and outside the cell are taken to be that of free water at ambient temperature: $D = 2 \cdot 10^{-9}$ m^2/s. We assume that the voxel size r_2 is 5 μm so that our system is originally a spherical bilayer structure. The permeability W_1 of the cellular membrane is 10^{-5} m/s. During the observation time t of *10* ms, the water protons travel on average distances around $\sqrt{Dt} \approx 4.47$ μm. In order to calculate the signal from this system, we introduce a supplementary layer of width σ. The permeability W_2 between the voxel and this layer is infinite because this virtual frontier goes across the same extracellular space. Finally, the permeability W_3 at the outer boundary of the supplementary layer is set to *0* (reflecting condition), although this value is irrelevant for computation. From a numerical point of view, one deals now with a spherical three-layered structure: the inner layer represents the cell, while the second and third layers represent the extracellular space.

Taking different values for σ, one can determine when the signal attenuation becomes independent of σ. As a benchmark, we consider the computation of the signal attenuation with $\sigma = 25$ μm which is approximately 5 times larger than the diffusion length $\sqrt{Dt}$. Fig. 7a shows the relative error of the signal attenuations for various σ, as compared to the reference signal attenuation (with $\sigma = 25$ μm). Even for $\sigma = 5$ μm, the maximal relative error is below 1%. The use of $\sigma = 10$ μm (which is approximately twice the diffusion length) gives very accurate results. Fig. 7a confirms that the presence of the fictitious boundary of the supplementary layer does not influence the signal attenuation inside the voxel.

Several technical comments are in order.

- The initial density $\rho(\mathbf{r})$ and the sampling function $\tilde{\rho}(\mathbf{r})$ are not uniform. In fact, we assumed that the nuclei are excited within the first two layers, i.e., $\rho(\mathbf{r}) = \mathbb{I}_{\Omega_0}(\mathbf{r})/V_0$, where $\Omega_0 = \Omega_1 \cup \Omega_2, V_0$ is the volume of these two layers Ω_1 and Ω_2, and $\mathbb{I}_A(\mathbf{r})$ is the indicator function: $\mathbb{I}_A(\mathbf{r}) = 1$ if $\mathbf{r} \in A$, and 0 otherwise. Similarly, the signal is formed by the nuclei which are located inside Ω_0 at time t, i.e., $\tilde{\rho}(\mathbf{r}) = \mathbb{I}_{\Omega_0}(\mathbf{r})$. The elements of the vectors U and $\widetilde{U}$ have to be recomputed. For this purpose, one can still use Eq. (A.2) from Appendix A but the summation should go up to $\ell - 1$ instead of ℓ because the supplementary layer ℓ is excluded.
- When $\rho(\mathbf{r})$ and $\tilde{\rho}(\mathbf{r})$ were uniform and the outer boundaries were reflecting, the signal attenuation was normalized as

$$E(g = 0) = (Ue^{-\Lambda t}\widetilde{U}) = 1.$$

This normalization does not hold in the non-uniform case. In fact, $E(g = 0)$ is smaller than 1 because the nuclei which were excited inside the first two layers, can leave this domain and thus diminish contributions to the signal. This "leakage" happens independently of the gradient strength. As a consequence, it is convenient to renormalize the signal by $E(g = 0)$, as one does in experiment when the signal is normalized by the reference signal. All the signal attenuations shown in Fig. 7 are normalized in this way.

As we mentioned at the beginning of this section, the permeability W_ℓ of the outer boundary was often used in order to account for one-way exchange with the extracellular space. It is instructive to compare the results for one-way and two-way exchanges. Fig. 7b shows the normalized signals from the above spherical bilayer structure. Blue solid curve shows the signal attenuation for two-way exchange which is obtained by our approach with the supplementary layer of width $\sigma = 25$ μm. This curve is referred to as the exact result. The dashed and dash-dotted lines present the signal attenuation for one-way exchange which is obtained by considering either fully reflecting ($W_2 = 0$), or fully absorbing ($W_2 = \infty$) outer boundary. One of these curves underestimates the signal attenuation, while the other overestimates it. Both approximations are inadequate. The last curve shown by circles was obtained manually by adjusting the permeability W_2 in order to get the closest representation of the solid line. Note that the optimal value $W_2 = 1.6 \cdot 10^{-3}$ m/s is too large for biological systems. We recall that the outer boundary of radius r_2 is a virtual frontier of the voxel that crosses the extracellular space. In other words, this optimal permeability does not have a physical meaning, it is just an effective value for getting the right result by using the wrong model. In turn, the introduction of a supplementary layer is a rigorous way to account for two-way exchange.

It is worth noting that the spectral approach developed in this paper is limited for studying a single multilayered structure. In practice, however, many copies of the same structure may be present. For instance, many living cells or axons are simultaneously present in the extracellular space. If these structures are close to each other, diffusive exchange between them may be relevant, and the present approach is not valid. If, on the opposite, these structures are relatively sparse so that the diffusive exchange between them can be neglected, the spectral approach can be applied.

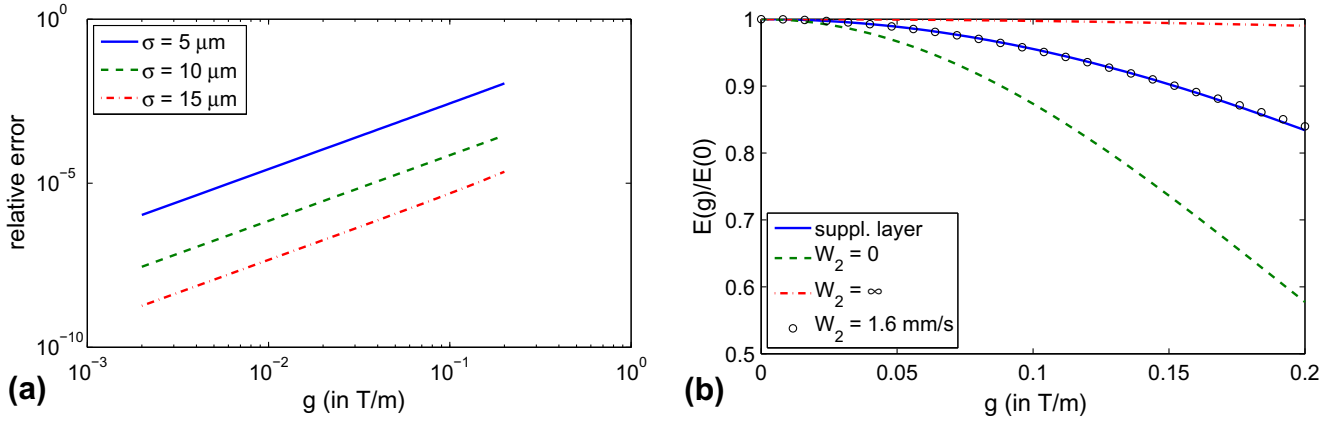

Fig. 7. Modeling the extracellular space. (a) The relative error of the signal for different widths σ of the supplementary layer which is added for modeling diffusion in the extracellular space. (b) Accurate computation of the signal attenuation and its approximations.

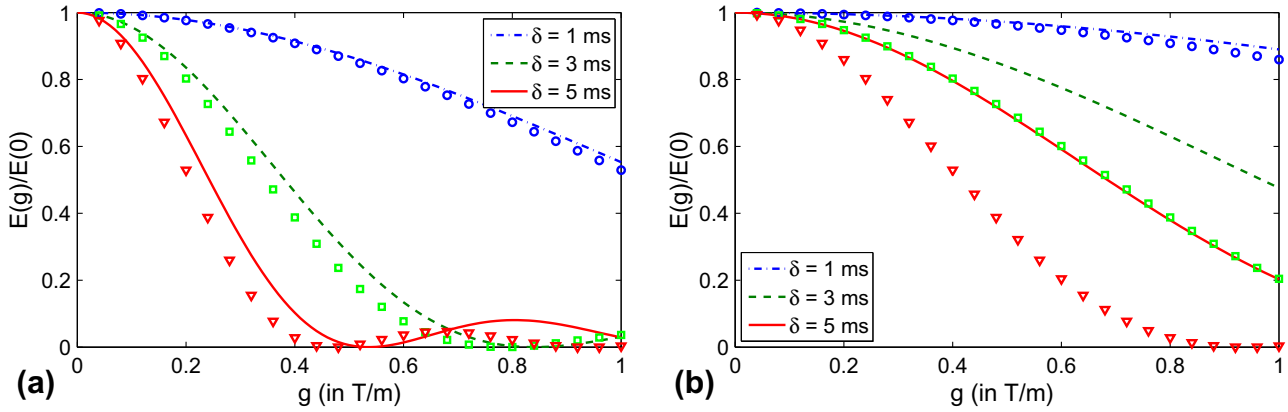

Fig. 8. Signal attenuation of water protons in a slab of width $R = 10$ μm (a) and $R = 5$ μm (b), with $D = 2 \cdot 10^{-9}$ m^2/s, $t = 50$ ms, and three values of the gradient duration δ. Lines show the signal attenuation computed by the matrix formalism, while symbols represent the NPA from Eq. (32): circles for $\delta = 1$ ms, squares for $\delta = 3$ ms, and triangles for $\delta = 5$ ms.

3.4. Narrow-pulse approximation

Many theoretical studies of the spin-echo signal attenuation relies on the narrow-pulse approximation (NPA) [60–63]. When the duration δ of the gradient pulses is short enough so that the motion of the nuclei during the time δ can be neglected, the signal attenuation can be approximated as

$$E_{NPA} = \int_\Omega d\mathbf{r}_0 \rho(\mathbf{r}_0) \int_\Omega d\mathbf{r}\; e^{2\pi i(\mathbf{q}\cdot\mathbf{r}_0)} G_t(\mathbf{r}_0, \mathbf{r}) e^{-2\pi i(\mathbf{q}\cdot\mathbf{r})},$$

where $\mathbf{q} = \gamma g \delta \mathbf{e}/(2\pi)$, and $G_t(\mathbf{r}_0,\mathbf{r})$ is the diffusive propagator describing the probability for a nucleus to move from $\mathbf{r}_0$ to $\mathbf{r}$ in time t (subject to appropriate boundary conditions). This relation states that the first gradient pulse (represented by $e^{2\pi i(\mathbf{q}\cdot\mathbf{r}_0)}$) at time 0 "encodes" the positions of the nuclei, while the second gradient pulse (represented by $e^{-2\pi i(\mathbf{q}\cdot\mathbf{r})}$) at time t allows to compare the actual position $\mathbf{r}$ to the initial position $\mathbf{r}_0$. The NPA becomes exact in the limit $\delta \to 0$ and $g \to \infty$ keeping $\mathbf{q}$ constant.

Assuming the uniform initial density $\rho(\mathbf{r}_0) = 1/Vol$ and using the spectral decomposition of the propagator on the basis of the Laplace operator eigenfunctions [11], one obtains

$$E_{NPA} = \sum_m V_m e^{-\lambda_m t} V_m^* = (V e^{-t\Lambda} V^*), \tag{32}$$

where

$$V_m = Vol^{-1/2} \int_\Omega d\mathbf{r}\; e^{2\pi i(\mathbf{q}\cdot\mathbf{r})} u_m(\mathbf{r}). \tag{33}$$

In Appendix A, the explicit formulas for the coefficients V_m are given in the case of multilayered structures. These formulas allow one for a rapid computation of the approximate signal attenuation E_{NPA}.

The narrow-pulse approximation is generally accepted as a reliable theoretical description of the spin-echo signal. However, the assumption of immobility of the nuclei during the gradient pulses is often not valid (see the review [11] and other references, e.g., [64,65]). This is particularly true for biological systems in which geometrical restrictions are in the order of microns. In order to illustrate this discrepancy, we compute the signal attenuation of water protons in a slab of width either $R = 10$ μm, or $R = 5$ μm (Fig. 8), by using the matrix formalism and the NPA. The gradient duration δ is varied between 1 ms and 5 ms, while the observation time t is set to 50 ms (the results are similar for $t = 20$ ms). For the shortest gradient duration $\delta = 1$ ms, the NPA (shown by circles) is rather accurate in both cases. For $R = 5$ μm, the signal remains almost unattenuated, $E(g = 1\ \text{T/m})/E(0) \approx 0.89$, so that an accurate characterization of the system is problematic. In order to overcome this difficulty, one can increase either the gradient strength, or the gradient duration. When $\delta = 3$ ms or 5 ms (squares and triangles, respectively), the NPA is still acceptable for $R = 10$ μm, although systematic deviations can already be observed. In turn, the NPA strongly overestimates the signal attenuation for $R = 5$ μm which is closer to the size of biological systems. For still smaller compartments (e.g., $R = 2$ μm, not shown), the NPA predictions are unacceptable.

Why does the NPA fail for small compartments? Although displacements of the nuclei during the gradient pulses, $\sqrt{D\delta} \approx 2.4$ μs (for $\delta = 3$ ms), are small in comparison to those during the observation time, $\sqrt{Dt} \approx 10$ μs, displacements in both cases are comparable to the compartment size R. The motional averaging leads therefore to a reduced "encoding strength" of the gradient pulses and, consequently, to less attenuated signals. The condition $\sqrt{D\delta} \ll R$, which turns out to be necessary for the applicability of the NPA, is restrictive for many biological systems.

4. Conclusion

Restricted diffusion was studied in several multilayered structures such as multiple slabs, cylindrical or spherical shells. Each layer could be characterized by its diffusion coefficient and bulk relaxation time, while the interlayer boundaries could be characterized by permeabilities. A new numerical algorithm for computing the signal attenuation due to linear magnetic field gradient and bulk relaxation was developed. This algorithm relied on the representation of the Bloch–Torrey equation on the explicitly known basis of the Laplace operator eigenfunctions. The spin-echo signal attenuation was written in a compact matrix form which was particularly suitable for numerical computations. The elements of the governing matrices were expressed in terms of the positive roots of explicit functions. A solution of the original sophisticated problem was therefore completely reduced to finding these roots. For rotation-invariant multilayered structures, the new matrix method was shown to be much more efficient, rapid and accurate than classical numerical techniques such as Monte Carlo simulations or finite-difference schemes. As an illustration of this method, the role of permeability of the intermediate boundary was investigated. The matrix formalism was implemented in Matlab, and the code is available on request. This code can be applied for studying restricted diffusion in biological systems, e.g., living cells (with three spherical shells representing a nucleus, a cytoplasm and an extracellular space), axons (with cylindrical shells) or composite tissues (with parallel slabs for each tissue component).

Acknowledgments

The author thanks Dr. I. Kezele for inspiring discussions about multilayered structures in biological and physiological systems. The work has been partly supported by the ANR program "DYOPTRI".

Appendix A. Computation of the integrals

The computation of the vectors $U, \widetilde{U}$ and matrices $\mathscr{B}, \mathscr{B}^{\mathrm{r}}$ for multilayered structures relies on several integrals involving the solutions of Eq. (9). As first shown in [11], these integrals can be computed explicitly. This is the key point for the efficiency of the spectral technique. In this Appendix, we summarize the analytical formulas for these integrals and describe the main steps of their derivation, following the ideas in [39].

Eq. (9) for the radial dependence $v(r)$ of a Laplace operator eigenfunction is

$$(r^{d-1}v')' + (\mu r^{d-1} - \nu r^{d-3})v = 0, \tag{A.1}$$

where μ is related to the eigenvalue of the Laplace operator, while ν is the eigenvalue of the corresponding Laplace–Beltrami operator (the angular part): $\nu = 0$ ($d = 1$), $\nu = n^2$ ($d = 2$), and $\nu = n(n+1)$ ($d = 3$).

A.1. Vector U for the uniform density

When the initial density $\rho(\mathbf{r})$ is uniform, the integral in Eq. (20) is split in radial and angular parts, the latter giving $\delta_{n,0}$ because of the rotation invariance. The radial integral

$$J_k \equiv \frac{1}{R^d - r_0^d}\int_{r_0}^{R} dr\; r^{d-1} v_{0k}(r)$$

can be separately evaluated on each layer. In fact, the integration of Eq. (A.1) with $\nu = 0$ over any interval $[a,b]$ yields

$$\int_a^b dr r^{d-1} v = -\frac{1}{\mu}\left[r^{d-1}v'\right]_a^b,$$

where $[f(r)]_a^b$ denotes the difference $f(b) - f(a)$. Applying this formula for each layer, one finds

$$\begin{aligned} J_k &= -\frac{1}{\lambda_{0k}(R^d - r_0^d)}\sum_{i=1}^{\ell} D_i\left[r_i^{d-1}v'_{i+1}(r_i) - r_{i-1}^{d-1}v'_{i+1}(r_{i-1})\right] \\ &= -\frac{1}{\lambda_{0k}(R^d - r_0^d)}\left[D_\ell R^{d-1}v'_{0k}(R) - D_1 r_0^{d-1}v'_{0k}(r_0)\right] \\ &= \frac{1}{\lambda_{0k}(R^d - r_0^d)}\left[W_\ell R^{d-1}v_{0k}(R) + W_0 r_0^{d-1}v_{0k}(r_0)\right]. \end{aligned} \tag{A.2}$$

The second equality relies on the boundary conditions on the intermediate frontiers, while the last equality is based on boundary conditions on the inner and outer frontiers. Note that this relation is independent of the permeabilities W_i of the intermediate boundaries. In particular, when the inner and outer frontiers are fully reflecting ($W_0 = W_\ell = 0$), one gets $J_k = 0$ (for $k > 0$), and $U_{nk} = \delta_{n,0}\delta_{k,0}$.

If $\lambda_{00} = 0$, the ground eigenfunction is constant, $v_{00}(r) = 1$, so that $J_0 = 1/d$.

A.2. Normalization constants and relaxation matrix

The elements of the relaxation matrices $\mathscr{B}^i$ involve the radial integrals

$$I_{nkk',i} \equiv \frac{1}{R^d - r_0^d}\int_{r_{i-1}}^{r_i} dr\; r^{d-1} v_{nk}(r) v_{nk'}(r).$$

The same type of integrals appears in the normalization constants β_{nk}:

$$\beta_{nk}^{-2} = \frac{2}{R^d - r_0^d}\int_{r_0}^{R} dr\; r^{d-1}[v_{nk}(r)]^2 = 2\sum_{i=1}^{\ell} I_{nkk,i} \equiv 2I_{nk}. \tag{A.3}$$

For the sake of simplicity, let us denote the functions $v_{nk}(r)$ and $v_{nk'}(r)$ as v_1 and v_2.

When $k \neq k'$, v_1 and v_2 are two solutions of Eq. (A.1) with different μ_1, μ_2, and the integration by parts yields

$$\begin{aligned} (\mu_1 - \mu_2)\int_a^b dr\; r^{d-1} v_1 v_2 &= (\nu_1 - \nu_2)\int_a^b dr\; r^{d-3} v_1 v_2 \\ &\quad - \left[r^{d-1}(v_1' v_2 - v_1 v_2')\right]_a^b. \end{aligned}$$

Since $\nu_1 = \nu_2$ (the same n for v_{nk} and $v_{nk'}$), the first term in the right-hand side is zero, and

$$\int_a^b dr\; r^{d-1} v_1 v_2 = \frac{1}{\mu_2 - \mu_1}\left[r^{d-1}(v_1' v_2 - v_1 v_2')\right]_a^b. \tag{A.4}$$

As a consequence, one finds

$$I_{nkk',i} = \frac{1}{R^d - r_0^d}\left[I_{nkk',i}(r_i) - I_{nkk',i}(r_{i-1})\right],$$

where the function $I_{nkk',i}(r)$ is

$$I_{nkk',i}(r) = \frac{D_i r^{d-1}}{\lambda_{nk'} - \lambda_{nk}}\left[v'_{nk,i}(r) v_{nk',i}(r) - v'_{nk',i}(r) v_{nk,i}(r)\right] \quad (k \neq k').$$

When $k = k'$, two integrations by parts are required for computing the integrals $I_{nkk,i}$. On one hand, multiplication of Eq. (A.1) by v and integration yield

$$\left[r^{d-1} v v'\right]_a^b + \mu\int_a^b dr\; r^{d-1} v^2 = \int_a^b dr\; r^{d-1}(v')^2 + \nu\int_a^b dr\; r^{d-3} v^2.$$

On the other hand, multiplication of the same Eq. (A.1) by rv' and integration give

$$\begin{aligned} 0 = &\left[r^d (v')^2 + \mu r^d v^2 - \nu r^{d-2} v^2\right]_a^b - \mu d\int_a^b dr\; r^{d-1} v^2 \\ &+ (d-2)\left[\int_a^b dr\; r^{d-1}(v')^2 + \nu\int_a^b dr\; r^{d-3} v^2\right], \end{aligned}$$

from which

$$\int_a^b dr\; r^{d-1} v^2 = \frac{1}{2\mu}\left[r^d (v')^2 + \mu r^d v^2 - \nu r^{d-2} v^2 + (d-2) r^{d-1} v v'\right]_a^b.$$

As a consequence,

$$\begin{aligned} I_{nkk,i}(r) = \frac{1}{2\lambda_{nk}}&\left[D_i r^d [v'_{nk,i}(r)]^2 + (\lambda_{nk} r^d - D_i r^{d-2}\nu_n)[v_{nk,i}(r)]^2\right. \\ &\left. + (d-2) D_i r^{d-1} v'_{nk,i}(r) v_{nk,i}(r)\right]. \end{aligned}$$

Finally, if $\lambda_{00} = 0$, the ground eigenfunction is constant, $v_{00}(r) = 1$, from which $I_{000,i}(r) = r^d/d$.

A.3. Matrix $\mathscr{B}$ for a linear gradient

The computation of the matrix $\mathscr{B}$ for a linear gradient involves the following integrals

$$K_{nk,n'k'} \equiv \frac{1}{L(R^d - r_0^d)}\int_{r_0}^{R} dr\; r^d v_{nk}(r) v_{n'k'}(r),$$

where L is the size of the multilayered structure (by convention, $L = R\text{-}r_0$ for $d = 1$, and $L = R$ for $d > 1$).

The computation relies on the same principles as earlier, although it is technically more difficult. We present only the main steps of computation.

For two solutions v_1 and v_2 of Eq. (A.1) with different μ_1, μ_2 and v_1, v_2, let us define

$$K = (\mu_1 - \mu_2)^2 \int_a^b dr\; r^{d-1+k} v_1 v_2,$$

where k is an integer ($k = 1$ for a linear gradient). The basic idea is to express $r^{d-1}\mu_i v_i$ by using Eq. (A.1) and then integrate by parts in order to "remove" derivatives. The first application of this idea yields

$$K = (\mu_1 - \mu_2)\left\{ \left[r^{d-1+k}(v_1 v_2' - v_1' v_2)\right]_a^b + (v_1 - v_2)\int_a^b dr\; r^{d-3+k} v_1 v_2 + k\int_a^b dr\; r^{d-2+k}(v_1' v_2 - v_1 v_2')\right\}.$$

After that, the factor $(\mu_1 - \mu_2)$ is again used to express $r^{d-1}\mu_i v_i$ according to Eq. (A.1) in the remaining integrals. Skipping technical details, we get

$$\begin{aligned} K = {} & \left[(\mu_1 - \mu_2) r^{d-1+k}(v_1 v_2' - v_1' v_2) + k(\mu_1 + \mu_2) r^{d-2+k} v_1 v_2 \right. \\ & - (v_1 - v_2 - k(d-2+k)) r^{d-3+k} v_1' v_2 \\ & - (v_2 - v_1 - k(d-2+k)) r^{d-3+k} v_1 v_2' \\ & \left. - k[v_1 + v_2 + (k-2)(d-2+k)] r^{d-4+k} v_1 v_2 + 2k r^{d-2+k} v_1' v_2' \right]_a^b \\ & + \left[(v_1 - v_2)^2 + k(k-2)(d-2+k)(d-4+k) - 2k(v_1 + v_2)\right] \\ & \times \int_a^b dr\; r^{d-5+k} v_1 v_2 + 2(v_1 - v_2)(k-1)\int_a^b dr\; r^{d-4+k} v_1' v_2 \\ & + 2(v_2 - v_1)(k-1)\int_a^b dr\; r^{d-4+k} v_1 v_2' - 4k(k-1)\int_a^b dr\; r^{d-3+k} v_1' v_2'. \end{aligned} \tag{A.5}$$

This formula was derived for $d = 2$ in [39]. In the particular case of $k = 1$ (linear gradient), the above expression is reduced to

$$\begin{aligned} K = {} & \left[(\mu_1 - \mu_2) r^d (v_1 v_2' - v_1' v_2) + (\mu_1 + \mu_2) r^{d-1} v_1 v_2 \right. \\ & - (v_1 - v_2 - (d-1)) r^{d-2} v_1' v_2 - (v_2 - v_1 - (d-1)) r^{d-2} v_1 v_2' \\ & \left. + 2r^{d-1} v_1' v_2' - (v_1 + v_2 - (d-1)) r^{d-3} v_1 v_2 \right]_a^b \\ & + \left[(v_1 - v_2)^2 - (d-1)(d-3) - 2(v_1 + v_2)\right]\int_a^b dr\; r^{d-4} v_1 v_2. \end{aligned} \tag{A.6}$$

In addition to explicit terms, this formula contains the integral which is unknown. However, the prefactor in front of this integral turns out to be 0 for the relevant cases:

- For $d = 1, v_1 = v_2 = 0$ so that the last term in Eq. (A.6) vanishes.
- For $d = 2$, one has $v_1 = n_1^2, v_2 = n_2^2$, where n_1 and n_2 are integer. Since the angular integral in Eq. (19) implies $|n_1 - n_2| = 1$, the prefactor in front of the last term in Eq. (A.6) is $(n_1 + n_2)^2 - 2(n_1^2 + n_2^2) + 1 = 0$.
- For $d = 3$, one has $v_1 = n_1(n_1 + 1), v_2 = n_2(n_2 + 1)$ and $|n_1 - n_2| = 1$, from which the last term vanishes.

As a result, we obtain for $n = n' \pm 1$ ($d > 1$) or $k \neq k'$ ($d = 1$),

$$K_{nk,n'k'} = \frac{1}{(\lambda_{nk} - \lambda_{n'k'})^2 L(R^d - r_0^d)} \sum_{i=1}^{\ell} \left[K_{nk,n'k',i}(r_i) - K_{nk,n'k',i}(r_{i-1})\right],$$

where

$$\begin{aligned} K_{nk,n'k',i}(r) = {} & \left[D_i(\lambda_{nk} + \lambda_{n'k'}) r^{d-1} - D_i^2(v_n + v_{n'} - (d-1)) r^{d-3}\right] v_{nk,i}(r) v_{n'k',i}(r) \\ & + \left[D_i(\lambda_{n'k'} - \lambda_{nk}) r^{d} - D_i^2(v_n - v_{n'} - (d-1)) r^{d-2}\right] v_{nk,i}'(r) v_{n'k',i}(r) \\ & + \left[D_i(\lambda_{nk} - \lambda_{n'k'}) r^{d} - D_i^2(v_{n'} - v_n - (d-1)) r^{d-2}\right] v_{nk,i}(r) v_{n'k',i}'(r) \\ & + 2D_i^2 r^{d-1} v_{nk,i}'(r) v_{n'k',i}'(r). \end{aligned}$$

In the one-dimensional case ($d = 1$), there is no condition $|n_1 - n_2| = 1$, and one needs to compute the diagonal elements of the matrix $\mathscr{B}$. In this case, Eq. (A.1) is simply $v'' + \mu v = 0$. On one hand, multiplication of this equation by rv and integration yield

$$\mu\int_a^b dr\; r v^2 - \int_a^b dr\; r(v')^2 = \left[v^2/2 - r v v'\right]_a^b.$$

On the other hand, its multiplication by $r^2 v'$ and integration give

$$\mu\int_a^b dr\; r v^2 + \int_a^b dr\; r(v')^2 = \left[r^2(v')^2/2 + \mu r^2 v^2/2\right]_a^b,$$

from which

$$\int_a^b dr\; r v^2 = \frac{1}{2\mu}\left[r^2(v')^2/2 + \mu r^2 v^2/2 + v^2/2 - r v v'\right]_a^b.$$

As a result, one finds for $d = 1$

$$\begin{aligned} K_{0k,0k} &= \frac{1}{L(R - r_0)}\int_{r_0}^R dr\; r v_{0k}^2(r) \\ &= \frac{1}{4\lambda_{0k} L(R - r_0)} \sum_{i=1}^{\ell} \left[K_{0k,0k,i}(r_i) - K_{0k,0k,i}(r_{i-1})\right] \end{aligned}$$

$$K_{0k,0k,i}(r) = D_i r^2 [v_{0k}'(r)]^2 + (\lambda_{0k} r^2 + D_i)[v_{0k}(r)]^2 - 2D_i r v_{0k}(r) v_{0k}'(r).$$

Finally, when $d = 1$ and $\lambda_{00} = 0$, one gets $K_{00,00} = (R + r_0)/(2L)$.

A.4. Coefficients for the narrow-pulse approximation

The coefficients in Eq. (32) can be computed exactly in the case of the multilayered structures. We consider three cases $d = 1$, $d = 2$ and $d = 3$ separately. In this Appendix, we replace $2\pi q$ by q to lighten expressions.

In one dimension, the coefficients are

$$V_{0k} = \frac{\sqrt{2}\beta_{0k}}{R - r_0}\int_{r_0}^R dr\; e^{iqr} v_{0k}(r).$$

Since both functions e^{iqr} and $v_{0k}(r)$ satisfy the differential Eq. (A.1), Eq. (A.4) yields

$$V_{0k} = \sqrt{2}\beta_{0k}\sum_{i=1}^{\ell}\left[V_{0k,i}(r_i) - V_{0k,i}(r_{i-1})\right],$$

where

$$V_{0k,i}(r) = \frac{1}{(q^2 - \lambda_{nk}/D_i)(R - r_0)}\left[v_{0k,i}'(r) e^{iqr} - v_{0k,i}(r)(iq e^{iqr})\right].$$

In two and three dimensions, one has

$$\begin{aligned} V_{nk} &= \frac{\varepsilon_n \beta_{nk}}{\pi(R^2 - r_0^2)}\int_{r_0}^R dr\; r v_{nk}(r)\int_0^{2\pi} d\theta \cos n\theta e^{iqr\cos\theta} \\ &= \frac{2\varepsilon_n \beta_{nk} i^n}{R^2 - r_0^2}\int_{r_0}^R dr\; r v_{nk}(r) J_n(qr) \quad (d = 2), \\ V_{nk} &= \frac{\sqrt{3/2}\beta_{nk}\sqrt{2n+1}}{R^3 - r_0^3}\int_{r_0}^R dr\; r^2 v_{nk}(r)\int_0^{\pi} d\theta \sin\theta P_n(\cos\theta) e^{iqr\cos\theta} \\ &= \sqrt{6}\sqrt{2n+1}\beta_{nk} i^n \frac{1}{R^3 - r_0^3}\int_{r_0}^R dr\; r^2 v_{nk}(r) j_n(qr) \quad (d = 3). \end{aligned}$$

Using again Eq. (A.4), one finds the general explicit formula for the coefficients V_{nk} for $d = 1,2,3$:

$$V_{nk} = \beta_{nk} \sum_{i=1}^{\ell} [V_{nk,i}(r_i) - V_{nk,i}(r_{i-1})], \tag{A.7}$$

where

$$V_{nk,i}(r) = \frac{r^{d-1}}{(q^2 - \lambda_{nk}/D_i)(R^d - r_0^d)} \left[v'_{nk,i}(r)\, \hat{v}_n(qr) - v_{nk,i}(r) q \hat{v}'_n(qr) \right], \tag{A.8}$$

and

$$\hat{v}_n(z) = \begin{cases} \sqrt{2} e^{iz} & (d = 1), \\ 2\varepsilon_n i^n J_n(z) & (d = 2), \\ \sqrt{6}\sqrt{2n+1}\, i^n j_n(z) & (d = 3). \end{cases} \tag{A.9}$$

Although the curves on Fig. 5b were plotted by using the matrices of size 100×100, the truncation to the size 10×10 shown here yields the green dashed line within relative errors less than 1% for the whole range of the b-value shown on Fig. 5b. Moreover, the truncation to the size 3×3 gives the same accuracy for the blue solid curve! This seemingly striking result has a simple explanation. Since the matrix $\mathscr{B}$ is a kind of perturbation of the matrix Λ, the truncation error is related to the "smallness" of $\omega\mathscr{B}$ in comparison to Λ. For the blue solid curve, the largest eigenvalue of the corresponding matrix 10Λ truncated to the size 3×3 is 575.11. This value is in the same order as the largest eigenvalue 445.47 of the matrix Λ truncated to the size 10×10 for the green dashed line, yielding thus similar accuracy. In general, smaller matrices are needed for computing the signal attenuation for faster diffusion.

$$\Lambda = \begin{pmatrix} 0 & 0 & 0 & 0 & 0 & 0 & 0 & 0 & 0 & 0 \\ 0 & 14.681 & 0 & 0 & 0 & 0 & 0 & 0 & 0 & 0 \\ 0 & 0 & 57.511 & 0 & 0 & 0 & 0 & 0 & 0 & 0 \\ 0 & 0 & 0 & 125.311 & 0 & 0 & 0 & 0 & 0 & 0 \\ 0 & 0 & 0 & 0 & 214.264 & 0 & 0 & 0 & 0 & 0 \\ 0 & 0 & 0 & 0 & 0 & 321.452 & 0 & 0 & 0 & 0 \\ 0 & 0 & 0 & 0 & 0 & 0 & 326.980 & 0 & 0 & 0 \\ 0 & 0 & 0 & 0 & 0 & 0 & 0 & 344.788 & 0 & 0 \\ 0 & 0 & 0 & 0 & 0 & 0 & 0 & 0 & 399.041 & 0 \\ 0 & 0 & 0 & 0 & 0 & 0 & 0 & 0 & 0 & 445.470 \end{pmatrix}$$

$$\mathscr{B} = \begin{pmatrix} 0 & 0.5517 & 0 & 0 & 0 & 0 & 0 & -0.0895 & 0 & 0 \\ 0.5517 & 0 & 0.3944 & 0 & 0 & 0 & -0.1085 & 0 & -0.0498 & 0 \\ 0 & 0.3944 & 0 & 0.4024 & 0 & 0 & 0 & -0.0881 & 0 & 0 \\ 0 & 0 & 0.4024 & 0 & 0.4125 & 0 & 0 & 0 & -0.0951 & 0 \\ 0 & 0 & 0 & 0.4125 & 0 & 0.4228 & 0 & 0 & 0 & 0 \\ 0 & 0 & 0 & 0 & 0.4228 & 0 & 0 & 0 & 0 & 0.4317 \\ 0 & -0.1085 & 0 & 0 & 0 & 0 & 0 & 0.5176 & 0 & 0 \\ -0.0895 & 0 & -0.0881 & 0 & 0 & 0 & 0.5176 & 0 & 0.3620 & 0 \\ 0 & -0.0498 & 0 & -0.0951 & 0 & 0 & 0 & 0.3620 & 0 & 0 \\ 0 & 0 & 0 & 0 & 0 & 0.4317 & 0 & 0 & 0 & 0 \end{pmatrix} \tag{B.1}$$

These formulas extend the classical results for a slab, a cylinder and a sphere [60,66–69].

Appendix B. Example of the matrices

As an illustration for the use of the matrix formalism, Eq. (B.1) gives explicitly the truncated matrices Λ and $\mathscr{B}$ of size 10×10 which allow one to draw the curves on Fig. 5b for the outer cylindrical shell of radii $r_1 = 2.5$ μm and $r_2 = 5$ μm with reflecting boundaries (note that $U_m = \widetilde{U}_m = \delta_{m,0}$). Fig. 5b illustrates two choices of the diffusion coefficient: $D = 2 \cdot 10^{-9}$ m^2/s (blue solid line) and $D = 2 \cdot 10^{-10}$ m^2/s (green dashed line). For a single-layer structure, the matrix $\mathscr{B}$ is independent of D, while the matrix Λ is proportional to D. The matrix Λ in Eq. (B.1) corresponds to the green dashed line, while the matrix 10Λ corresponds to the blue solid line.

References

[1] P.T. Callaghan, Principles of Nuclear Magnetic Resonance Microscopy, Clarendon Press, Oxford, 1991.
[2] A.T. Watson, C.T.P. Chang, Characterizing porous media with NMR methods, Prog. Nucl. Magn. Reson. Spectrosc. 31 (1997) 343–386.
[3] P.J. Barrie, Characterization of porous media using NMR methods, Annu. Rep. NMR Spectrosc. 41 (2000) 265–316.
[4] W.S. Price, NMR Studies of Translational Motion: Principles and Applications, Cambridge University Press, Cambridge, 2009.
[5] D. Le Bihan, Looking into the functional architecture of the brain with diffusion MRI, Nat. Rev. Neurosci. 4 (2003) 469–480.
[6] L. Minati, W.P. Weglarz, Physical foundations, models, and methods of diffusion magnetic resonance imaging of the brain: a review, Concept Magn. Reson. 30 A (2007) 278–307.
[7] H.E. Möller, X.J. Chen, B. Saam, K.D. Hagspiel, G.A. Johnson, T.A. Altes, E.E. de Lange, H.-U. Kauczor, MRI of the lungs using hyperpolarized noble gases, Magn. Reson. Med. 47 (2002) 1029–1051.
[8] E.J.R. van Beek, J.M. Wild, H.-U. Kauczor, W. Schreiber, J.P. Mugler, E.E. de Lange, Functional MRI of the lung using hyperpolarized 3-helium gas, J. Magn. Reson. Imag. 20 (2004) 540–554.

[9] S.J. Kadlecek, K. Emami, M.C. Fischer, M. Ishii, J. Yu, J.M. Woodburn, M. NikKhah, V. Vahdat, D.A. Lipson, J.E. Baumgardner, R.R. Rizi, Imaging physiological parameters with hyperpolarized gas MRI, Prog. Nucl. Magn. Reson. Spectrosc. 47 (2005) 187–212.
[10] M.S. Conradi, B. Saam, D.A. Yablonskiy, J.C. Woods, Hyperpolarized 3He and perfluorocarbon gas diffusion MRI of lungs, Prog. Nucl. Magn. Reson. Spectrosc. 48 (2006) 63–83.
[11] D.S. Grebenkov, NMR survey of reflected Brownian motion, Rev. Mod. Phys. 79 (2007) 1077–1137.
[12] C.D. Araujo, A.L. Mackay, K.P. Whittall, J.R.T. Hailey, A diffusion model for spin–spin relaxation of compartmentalized water in wood, J. Magn. Reson. B 101 (1993) 248–261.
[13] M. Peyron, G.K. Pierens, A.J. Lucas, L.D. Hall, R.C. Stewart, The modified stretched-exponential model for characterization of NMR relaxation in porous media, J. Magn. Reson. A 118 (1996) 214–220.
[14] K.M. Bennett, K.M. Schmainda, R. Bennett, D.B. Rowe, H. Lu, J.S. Hyde, Characterization of continuously distributed cortical water diffusion fates with a stretched-exponential model, Magn. Reson. Med. 50 (2003) 727–734.
[15] T. Niendorf, R.M. Dijkhuizen, D.G. Norris, M. van Lookeren Campagne, K. Nicolay, Biexponential diffusion attenuation in various states of brain tissue: implications for diffusion-weighted imaging, Magn. Reson. Med. 36 (1996) 847–857.
[16] R.V. Mulkern, H. Gudbjartsson, C.F. Westin, H.P. Zengingonul, W. Gartner, C.R. Guttmann, Multicomponent apparent diffusion coefficients in human brain, NMR Biomed 12 (1999) 51–62.
[17] C.A. Clark, D. Le Bihan, Water diffusion compartmentation and anisotropy at high *b* values in the human brain, Magn. Reson. Med. 44 (2000) 852–859.
[18] J.V. Sehy, J.J.H. Ackerman, J.J. Neil, Evidence that both fast and slow water ADC components arise from intracellular space, Magn. Reson. Med. 48 (2002) 765–770.
[19] G.J. Stanisz, A. Szafer, G.A. Wright, R.M. Henkelman, An analytical model of restricted diffusion in bovine optic nerve, Magn. Reson. Med. 37 (1997) 103–111.
[20] G.J. Stanisz, Diffusion MR in biological systems: tissue compartments and exchange, Isr. J. Chem. 43 (2003) 33–44.
[21] A. Caspi, R. Granek, M. Elbaum, Enhanced diffusion in active intracellular transport, Phys. Rev. Lett. 85 (2000) 5655–5658.
[22] D. Arcizet, B. Meier, E. Sackmann, J.O. Radler, D. Heinrich, Temporal analysis of active and passive transport in living cells, Phys. Rev. Lett. 101 (2008) 248103.
[23] J.-P. Bouchaud, A. Georges, Anomalous diffusion in disordered media: statistical mechanisms, models and physical applications, Phys. Rep. 195 (1990) 127–293.
[24] R. Metzler, J. Klafter, The random walk's guide to anomalous diffusion: a fractional dynamics approach, Phys. Rep. 339 (2000) 1–77.
[25] S. Havlin, D. Ben-Avraham, Diffusion in disordered media, Adv. Phys. 51 (2002) 187–292.
[26] R. Kimmich, Strange kinetics, porous media, and NMR, Chem. Phys. 284 (2002) 253–285.
[27] D.S. Grebenkov, Laplacian eigenfunctions in NMR I. A numerical tool, Concept Magn. Reson. A 32 (2008) 277–301.
[28] D.S. Grebenkov, Laplacian eigenfunctions in NMR. II theoretical advances, Concept Magn. Reson. A 34 (2009) 264–296.
[29] H. Flanders, Differential Forms with Applications to the Physical Sciences, Dover, New York, 1989.
[30] B. Robertson, Spin-echo decay of spins diffusion in a bounded region, Phys. Rev. 151 (1966) 273–277.
[31] A. Caprihan, L.Z. Wang, E. Fukushima, A Multiple-narrow-pulse approximation for restricted diffusion in a time-varying field gradient, J. Magn. Reson. A 118 (1996) 94–102.
[32] P.T. Callaghan, A simple matrix formalism for spin echo analysis of restricted diffusion under generalized gradient waveforms, J. Magn. Reson. 129 (1997) 74–84.
[33] A.V. Barzykin, Exact solution of the Torrey–Bloch equation for a spin echo in restricted geometries, Phys. Rev. B 58 (1998) 14171–14174.
[34] A.V. Barzykin, Theory of spin echo in restricted geometries under a step-wise gradient pulse sequence, J. Magn. Reson. 139 (1999) 342–353.
[35] S.L. Codd, P.T. Callaghan, Spin echo analysis of restricted diffusion under generalized gradient waveforms: planar, cylindrical and spherical pores with wall relaxivity, J. Magn. Reson. 137 (1999) 358–372.
[36] S. Axelrod, P.N. Sen, Nuclear magnetic resonance spin echoes for restricted diffusion in an inhomogeneous field: methods and asymptotic regimes, J. Chem. Phys. 114 (2001) 6878–6895.
[37] D.S. Grebenkov, NMR restricted diffusion between parallel planes in a cosine magnetic field: an exactly solvable model, J. Chem. Phys. 126 (2007) 104706.
[38] D.S. Grebenkov, Multiple correlation function approach: rigorous results for simple geometries, Diffus. Fundam. 5 (2007) 1–34.
[39] D.S. Grebenkov, Analytical solution for restricted diffusion in circular and spherical layers under inhomogeneous magnetic fields, J. Chem. Phys. 128 (2008) 134702.
[40] E. Özarslan, Compartment shape anisotropy (CSA) revealed by double pulsed field gradient MR, J. Magn. Reson. 199 (2009) 56–67.
[41] N. Shemesh, E. Özarslan, A. Bar-Shir, P.J. Basser, Y. Cohen, Observation of restricted diffusion in the presence of a free diffusion compartment: single- and double-PFG experiments, J. Magn. Reson. 200 (2009) 214–225.
[42] E.L. Hahn, Spin echoes, Phys. Rev. 80 (1950) 580–594.
[43] H.Y. Carr, E.M. Purcell, Effects of diffusion on free precession in NMR experiments, Phys. Rev. 94 (1954) 630–638.
[44] K.R. Brownstein, C.E. Tarr, Importance of classical diffusion in NMR studies of water in biological cells, Phys. Rev. A 19 (1979) 2446–2453.
[45] J.E. Tanner, Transient diffusion in a system partitioned by permeable barriers. Application to NMR measurements with a pulsed field gradient, J. Chem. Phys. 69 (1978) 1748–1754.
[46] J. Andrasko, Water diffusion permeability of human erythrocytes studied by a pulsed gradient NMR technique, Biochim. Biophys. Acta 428 (1976) 304–311.
[47] P.W. Kuchel, A. Coy, P. Stilbs, NMR diffusion–diffraction of water revealing alignment of erythrocytes in a magnetic field and their dimensions and membrane transport characteristics, Magn. Reson. Med. 37 (1997) 637–643.
[48] A.V. Barzykin, K. Hayamizu, W.S. Price, M. Tachiya, Pulsed-field-gradient NMR of diffusive transport through a spherical interface into an external medium containing a relaxation agent, J. Magn. Reson. A 114 (1995) 39–46.
[49] W.S. Price, A.V. Barzykin, K. Hayamizu, M. Tachiya, A model for diffusive transport through a spherical interface probed by pulsed-field gradient NMR, Biophys. J. 74 (1998) 2259–2271.
[50] P.W. Kuchel, C.J. Durrant, Permeability coefficients from NMR q-space data: models with unevenly spaced semi-permeable parallel membranes, J. Magn. Reson. 139 (1999) 258–272.
[51] P.-C. Jiang, T.-Y. Yu, W.-C. Perng, L.-P. Hwang, Pore-to-pore hopping model for the interpretation of the pulsed gradient spin echo attenuation of water diffusion in cell suspension systems, Biophys. J. 80 (2001) 2493–2504.
[52] P.N. Sen, Time-dependent diffusion coefficient as a probe of permeability of the pore wall, J. Chem. Phys. 119 (2003) 9871–9876.
[53] P.N. Sen, Time-dependent diffusion coefficient as a probe of geometry, Concepts Magn. Reson. A23 (2004) 1–21.
[54] I. Kezele, P. Batchelor, C. Poupon, J-F. Mangin, D. Le Bihan, D.C. Alexander, Feasibility of measuring microstructural features of systems with intermediate exchange and sub-cellular compartmentalization using diffusion mri", in: Proceedings of ISMRM 10, 2010, 2377.
[55] C.H. Neuman, Spin echo of spins diffusion in a bounded medium, J. Chem. Phys. 60 (1974) 4508–4511.
[56] D.S. Grebenkov, Use, misuse and abuse of apparent diffusion coefficients, Concept Magn. Reson. A36 (2010) 24–35.
[57] D.S. Grebenkov, G. Guillot, B. Sapoval, Restricted diffusion in a model acinar labyrinth by NMR. Theoretical and numerical results, J. Magn. Reson. 184 (2007) 143–156.
[58] D.S. Grebenkov, M. Filoche, B. Sapoval, Spectral properties of the Brownian self-transport operator, Eur. Phys. J. B 36 (2003) 221–231.
[59] P.T. Callaghan, A. Coy, D. MacGowan, K.J. Packer, F.O. Zelaya, Diffraction-like effects in NMR diffusion studies of fluids in porous solids, Nature 351 (1991) 467–469.
[60] J.E. Tanner, E.O. Stejskal, Restricted self-diffusion of protons in colloidal systems by the pulsed-gradient, spin-echo method, J. Chem. Phys. 49 (1968) 1768–1777.
[61] W.S. Price, Pulsed-field gradient nuclear magnetic resonance as a tool for studying translational diffusion. Part 1. Basic theory, Concept Magn. Reson. 9 (1997) 299–336.
[62] W.S. Price, Pulsed-field gradient nuclear magnetic resonance as a tool for studying translational diffusion. Part 2. Experimental aspects, Concept Magn. Reson. 10 (1998) 197–237.
[63] P.T. Callaghan, S.L. Codd, J.D. Seymour, Spatial coherence phenomena arising from translational spin motion in gradient spin echo experiments, Concept Magn. Reson. 11 (1999) 181–202.
[64] W.S. Price, P. Stilbs, O. Söderman, Determination of pore space shape and size in porous systems using NMR diffusometry. Beyond the short gradient pulse approximation, J. Magn. Reson. 160 (2003) 139–143.
[65] W.S. Price, O. Söderman, Some "Reflections" on the effects of finite gradient pulse lengths in PGSE NMR experiments in restricted systems, Isr. J. Chem. 43 (2003) 25–32.
[66] A. Coy, P.T. Callaghan, Pulsed gradient spin echo nuclear magnetic resonance for molecules diffusing between partially reflecting rectangular barriers, J. Chem. Phys. 101 (1994) 4599–4609.
[67] P.T. Callaghan, Pulsed gradient spin echo NMR for planar, cylindrical and spherical pores under conditions of wall relaxation, J. Magn. Reson. A 113 (1995) 53–59.
[68] O. Söderman, B. Jönsson, Restricted diffusion in cylindrical geometry, J. Magn. Reson. A 117 (1995) 94–97.
[69] S.J. Gibbs, Observations of diffusive diffraction in a cylindrical pore by PFG NMR, J. Magn. Reson. 124 (1997) 223–226.